D.A. Dei Tos, M. Rasotto, F. Renk, F. Topputo
LISA Pathfinder Mission Extension: a Feasibility Analysis
Advances in Space Research, Vol. 63, N. 12, 2019, p. 3863-3883
doi:10.1016/j.asr.2019.02.035

LISA Pathfinder mission extension: A feasibility analysis

Diogene A. Dei Tos[1,]

Politecnico di Milano, via La Masa 34, 20156 Milan, Italy.

Mirco Rasotto[2,]

Dinamica Srl, Via Morghen 13, 20158 Milan, Italy.

Florian Renk[3,]

European Space Agency, ESOC, Robert-Bosch-Str., 64293 Darmstadt, Germany.

Francesco Topputo[4,*]

Politecnico di Milano, via La Masa 34, 20156 Milan, Italy.

Abstract

A proposed mission extension for LISA Pathfinder involved redirecting the probe to the Sun–Earth gravitational saddle point. Realistic models for both space and ground segments were used to carry out a number of analyses for trajectory design, orbit determination, and navigation cost. In this work, we present the methods that allow assessing the feasibility of flying general limited-control-authority spacecraft in highly nonlinear dynamics, and in particular of the proposed mission extension in a statistically reliable approach. Solutions for transfers from the Sun–Earth L_1 and L_2 to the saddle point

*Corresponding author

Email addresses: diogenealessandro.deitos@polimi.it (Diogene A. Dei Tos), rasotto@dinamicatech.com (Mirco Rasotto), florian.renk@esa.int (Florian Renk), francesco.topputo@polimi.it (Francesco Topputo)

[1]PostDoctoral Research Fellow, Department of Aerospace Science and Technology.

[2]Senior Engineer, Dinamica Srl.

[3]Mission Analyst, Mission Analysis Section, Flight Mechanics Division, Ground Systems Engineering Department.

[4]Assistant Professor, Department of Aerospace Science and Technology.

are shown, which feature very low Δv consumption, from few centimeters per second to 10 m/s. The analysis is then specialized to the case of LISA Pathfinder, for which several solutions are presented. This work gives evidence that LISA Pathfinder might have been able to fly-through the saddle point, provided initial tracking errors within 10 km in each position component and 0.1 m/s in each velocity component. A critical discussion on the opportunistic mission extension is eventually made.

Keywords: Low-thrust trajectory; Optimal trajectory design; Radiometric navigation; Lagrange point orbits; Gravitational saddle point; LISA Pathfinder.

1. Introduction

Since the launch of the International Sun–Earth Explorer in 1978 (Farquhar et al., 1980), the number of Lagrange point orbits (LPO) missions has increased over the last 15 years (Farquhar et al., 2004) and a further growth is expected within the next years. The main reasons behind the increasing interest in flying in highly nonlinear gravitational fields are due to the unique features that can be extracted if these models are properly exploited. LPO, ballistic capture orbits, low-energy transfers, and invariant manifolds are just mere examples of what can be done by using the natural motion of a spacecraft with proper energies in these environments (Topputo and Zhang, 2014). Beside generating orbits that cannot be designed in the classic two-body model, low-energy multi-body models may allow for saving considerable fractions of propellant, widening the launch windows, or increasing the safety of close approaches, as in the case of ballistic capture (Belbruno and Miller, 1993; Mingotti and Topputo, 2011; Topputo and Belbruno, 2015). This means that even spacecraft with very limited thrust authority may be able to accomplish orbital transfers that may seem unfeasible by far at a first glance (Dei Tos, 2018).

Recently, a number of studies assessed the feasibility of leveraging the highly nonlinear Sun–Earth–Moon environment to fly by the Sun–Earth gravitational saddle point (SP) region at affordable cost and duration (Trenkel and Kemble, 2009; Trenkel et al., 2012; Fabacher et al., 2013; Cox and Howell, 2016; Topputo et al., 2018b). Saddle points are defined as those locations in space where the net gravitational acceleration balances. Consequently, the saddle points present clean, close-to-zero background acceleration envi-

ronments where deviations from the General Relativity and Newton's gravitational law can be measured. As such, saddle points are intriguing the scientific community. More specifically, these regions represent a suitable environment to test the MOdified Newtonian Dynamics (MOND) theory, formulated by Milgrom (1983), and subsequently integrated in a relativistic complete theory, labelled as Tensor-Vector-Scalar gravity (TeVeS), by Bekenstein (2004). MOND is an alternative paradigm to Newtonian dynamics, originally formulated to explain anomalies in galaxies radial velocities without invoking non-baryonic dark matter. Figure 1 shows examples of MOND rotation curve analysis for three galaxies of very different types (Milgrom, 2008). This theory predicts that in those locations where the gravitational acceleration is below 10^{-10} m/s^2, the standard Newtonian dynamics needs to be modified (Milgrom, 1983). This may occur at the edge of galaxies, but anomalous MOND/TeVeS gravity gradients greater than $\geq 10^{-13}$ s^{-2} are also predicted within an elliptic bubble around the Sun–Earth saddle point (Trenkel and Wealthy, 2014), which is more accessible.

Among these remarkable and yet unexplored points, the Sun–Earth SP, located at a distance of approximately 258,800 km from the center of the Earth along the Sun–Earth line and between the Sun and the Earth, seems particularly appealing as it can be reached with ultra low-thrust missions, by exploiting the nonlinearity of the vector field (Topputo et al., 2018c; Dei Tos and Topputo, 2019). Nonetheless, 1) the high precision requirements in terms of accurate SP targeting (miss-distance < 50 km in Bekenstein and Magueijo (2006) and < 1 km in Galianni et al. (2012)), 2) the highly unstable dynamical environment, 3) the occurrence of solar conjunction (by definition of

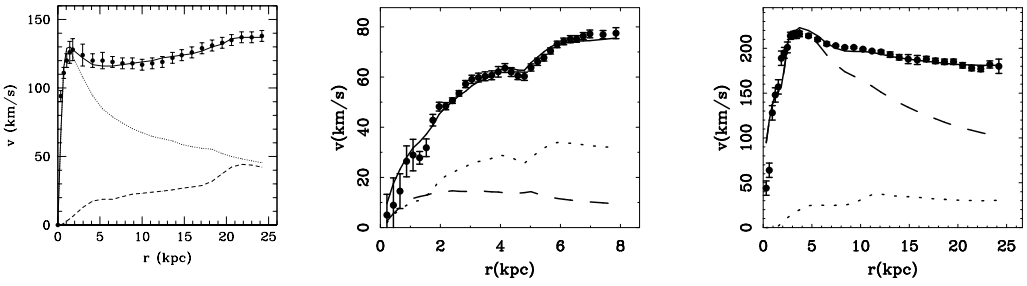

Figure 1: The observed and MOND rotation curves (in solid lines) for NGC 3657 (left), NGC 1560 (center), and NGC 2903 (right). The first from Sanders (2007), the last two from Sanders and McGaugh (2002). Dotted and dashed lines are the Newtonian curves calculated for the different baryonic components. Credits: Milgrom (2008).

SP), and 4) the need to perform multiple passages (to exclude false positives and have redundant measurements), represent strong constraints from the operational point of view, even more so for a spacecraft with limited control authority.

In this work, we develop efficient methodologies to design and navigate highly-nonlinear, control-limited orbits flying by the Sun–Earth saddle point and starting from Sun–Earth $L_{1,2}$ LPO. The focus is on solutions with very low Δv budget (1–10 m/s), ultra low thrust (0.1–10 mN), and low/medium resources spacecraft (200–2000 kg). Particular emphasis is put in the realization of maneuvers of finite burn duration, as opposed to impulsive maneuvers. This is because a 500 kg spacecraft equipped with cold gas thrusters able to provide 1 mN maximum thrust, values representative of LISA Pathfinder (LPF) at end of life (Landgraf et al., 2014), would require 5.78 days of continuous engine operation to impart a total Δv of 1 m/s. Thus, the use of impulsive maneuvers to control an ultra-low authority spacecraft may result in large errors and, in the worst case scenario, non-feasibility of the maneuver. It is then imperative to spread the impulsive Δv to finite-burn arcs. Numerical simulations show that converting impulsive maneuvers into finite burn arcs produces a satisfactory level of accuracy in the roto-pulsating restricted n-body problem (RPRnBP), a high-fidelity model stated in a synodic frame (Gómez et al., 2002; Dei Tos and Topputo, 2017, 2019).

In a second step, we assess the feasibility of flying such trajectories in a simulated environment. Radiometric measurements from an ESA/ESTRACK ground station are used as input for a refined orbit determination analysis. The flight dynamics cycle and operations are scheduled considering a wide array of constraints both on the space and ground segments; e. g., eclipses and occultations, impact of thruster outages, and attitude rates. The navigation cost is then estimated based on a linearized open-loop control strategy to track the reference orbit. Finally, optimal transfer cost and navigation cost of a set of transfers using LISA Pathfinder as test scenario are shown to demonstrate feasibility of the mission extension to the Sun–Earth saddle point. The methodologies described in this paper are implemented in the state-of-the-art Ultra-Low Thrust Interplanetary Mission Analysis Tool (ULTIMAT) developed at Politecnico di Milano, an engineering tool initiated under ESA Contract, the aim of which is performing trajectory optimization into highly nonlinear models, where the design is constrained from the very-limited control authority (Topputo et al., 2018a).

The remainder of the paper is organized as follows. Section 2 illustrates

the method to convert a series of impulsive maneuvers into a series of finite thrust arcs in a high-fidelity restricted rotating n-body model. Then, Section 3 describes techniques to assess the feasibility of computed trajectories with an orthodox navigation analysis. The results obtained for the case of LISA Pathfinder mission extension and for general LPO-to-SP transfers are presented in Section 4. Finally, Section 5 draws critical conclusions and set forward suggestions to fly very limited control authority spacecraft in highly nonlinear environments.

2. Impulsive to finite-burn maneuver conversion

An automated method is described that converts a single impulsive maneuver to a time optimal finite burn maneuver (FBM) for a thrust limited, constant exhaust velocity rocket engine (ideal engine performances). The equations of motion for a thrusting spacecraft are

$$\dot{\boldsymbol{X}} = \boldsymbol{f}(t, \boldsymbol{X}, \boldsymbol{\vartheta}, u, \alpha, \beta) := \begin{cases} \dot{\boldsymbol{r}} = \boldsymbol{v} \\ \dot{\boldsymbol{v}} = \boldsymbol{g}(t, \boldsymbol{r}, \boldsymbol{v}, \boldsymbol{\vartheta}) + \dfrac{uT_{\max}}{m}\boldsymbol{\gamma}(\alpha, \beta) \\ \dot{m} = -\dfrac{uT_{\max}}{c_e} \end{cases} \tag{1}$$

where $\boldsymbol{X} = [\boldsymbol{r}^\top, \boldsymbol{v}^\top, m]^\top$ is the spacecraft state, made of position ($\boldsymbol{r}$), velocity ($\boldsymbol{v}$), and mass (m); $\boldsymbol{g}$ is the acceleration field considered; t is the time; $\boldsymbol{\vartheta}$ is a vector of parameters; $T_{\max}$ is the maximum available thrust; $c_e = I_{sp}\, g_0$ is the engine exhaust speed (where I_{sp} is its specific impulse and g_0 the gravitational acceleration at sea level); $u \in [0, 1]$ is the throttle factor; $\boldsymbol{\gamma}(\alpha, \beta) := [\cos\beta\cos\alpha, \cos\beta\sin\alpha, \sin\beta]^\top$ is the thrust pointing direction, where $\alpha \in [0, 2\pi]$ is the thrust azimuth angle and $\beta \in [-\pi/2, \pi/2]$ is the thrust elevation angle, defined with respect to the same reference frame Eqs. (1) are cast. Accordingly, the thrust vector yields $\boldsymbol{T} = uT_{\max}\boldsymbol{\gamma}$. The control parameters are $u(t)$, $\alpha(t)$, and $\beta(t)$. In this work, we assume an ideal engine with $T_{\max} = \text{const}$, $c_e = \text{const}$.

Within the impulsive maneuver paradigm, an maneuver produces instantaneous known variations of velocity and mass,

$$\boldsymbol{v}^+ = \boldsymbol{v}^- + \Delta\boldsymbol{v}, \qquad \Delta m = m^+ - m^- = m^-\left(e^{-\|\Delta\boldsymbol{v}\|/c_e} - 1\right), \tag{2}$$

where $(\cdot)^-$ and $(\cdot)^+$ indicates pre- and post-impulse quantities, respectively, and $\Delta\boldsymbol{v}$ is the instantaneous velocity change vector.

An impulsive-to-finite-burn maneuver conversion produces a finite burn solution whose final position and velocity are equal to the final position and velocity of the original post-impulse trajectory at the time the finite burn maneuver ends. The single impulsive maneuver may be part of a more complex multi-impulse trajectory. The goal is to convert each impulse to a finite-burn maneuver so that the resulting multi-finite-burn maneuver trajectory satisfies the mission requirements of the original impulsive trajectory. Thus, the coast phases of the impulsive and finite burn trajectories are equal. In this work, each impulsive maneuver is converted separately. It is assumed that the end time of a finite burn maneuver is less than or equal to the start time of the next finite burn maneuver that is used to replace the next impulsive maneuver, if any.

The finite burn maneuver conversion for a single impulse is treated as a pseudo-rendezvous problem where the target particle flies along the post-impulse trajectory (Ocampo and Munoz, 2010). The conversion is carried out in a time optimal sense. The time of the impulse is t_i, and the state on the finite burn trajectory is calculated in the epoch interval $[t_0, t_f]$, with $t_0 < t_i < t_f$. Referring to Figure 2, the pre-impulse ballistic trajectory is defined as a continuous trajectory from t_0 to t_f (dashed line in Figure 2). The post-impulse ballistic trajectory is defined by two continuous ballistic arcs that have initial state $\boldsymbol{r}_i$, $\boldsymbol{v}_i^+$, m_i^+ at t_i (dashed-dotted line in Figure 2). The first one is a backward propagated ballistic arc from t_i to t_0 and the second one is a forward propagated ballistic arc from t_i to t_f. Refer to the particles on the pre-impulse and post-impulse trajectories as the chase and target particles, respectively. The impulse is to be replaced by a finite burn maneuver with known control parameters history. Thus, the chase particle is the spacecraft itself that flies along the pre-impulse trajectory and is required to rendezvous with the target particle.

The problem of converting an impulsive maneuver to a finite-burn arc is now formally stated.

Problem 1. *Find* $\{u(t), \alpha(t), \beta(t), t_0, t_f\}$ *such that*

$$\boldsymbol{r}(t_0) = \bar{\boldsymbol{r}}(t_0), \quad \boldsymbol{v}(t_0) = \bar{\boldsymbol{v}}(t_0), \quad \boldsymbol{r}(t_f) = \boldsymbol{r}^*(t_f), \quad \boldsymbol{v}(t_f) = \boldsymbol{v}^*(t_f), \tag{3}$$

where t_0 *and* t_f *are the times when the finite burn starts and ends, respectively (see Figure 2),* $\boldsymbol{r}$*,* $\boldsymbol{v}$ *are the position and velocity vectors along the finite burn arc, barred quantities (*$\bar{\boldsymbol{r}}$*,* $\bar{\boldsymbol{v}}$*) represent position and velocity along the*

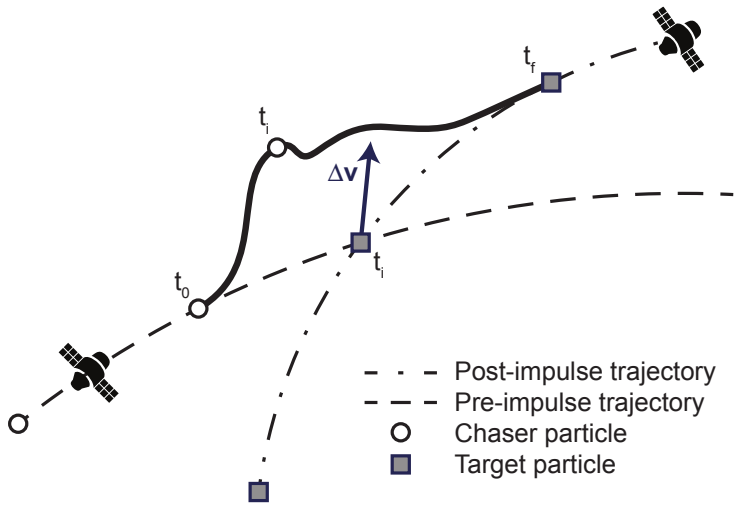

Figure 2: Geometry of impulsive to finite burn maneuver pseudo-rendezvous.

pre-impulse trajectory, and starred quantities ($\boldsymbol{r}^*$, $\boldsymbol{v}^*$) *represent position and velocity along the post-impulse trajectory.*

Problem 1 is applied to one impulsive maneuver, and can be readily generalized for n other impulses, provided they are dealt with separately.

2.1. Direct finite burn control model

To reduce the search space and transition to a simpler mathematical problem we make the following considerations valid for $t \in [t_0, t_f]$:

1. For minimum time finite burn problem we have (Senent et al., 2005)

$$u = 1 \qquad \Longrightarrow \qquad \|\boldsymbol{T}\| = T_{\max}. \tag{4}$$

2. The thrust azimuth and elevation angles are approximated as cubic polynomials of time with unknown coefficients $\{a_j, b_j\}$, i. e.,

$$\alpha(t) = \sum_{j=0}^{3} a_j \frac{(t-t_i)^j}{j!}, \qquad \beta(t) = \sum_{j=0}^{3} b_j \frac{(t-t_i)^j}{j!}. \tag{5}$$

   Third-order polynomials centered at the impulsive maneuver epoch are preferred over more refined interpolating techniques, such as Legendre-Gauss or Gauss-Lobatto, because a straightforward physical interpretation is given to the coefficients and the initial estimation favors convergence (see Section 2.2.2.)

These considerations (the first being an established result, and the second a convenient approximation) translate the finite burn conversion problem into finding 8 constant control parameters (coefficients of the cubic polynomials representing the thrust spherical angles) and 2 engine switching epochs (on and off). There are 10 decision variables per maneuver, collected in the vector

$$\boldsymbol{s} = (t_0, t_f, a_0, a_1, a_2, a_3, b_0, b_1, b_2, b_3)^\top. \tag{6}$$

Problem 2. *Let the scaled duration of the finite-burn arc,*

$$J(\boldsymbol{s}) = k(t_f - t_0), \tag{7}$$

represent the cost function, and let

$$\boldsymbol{l}(\boldsymbol{s}) = \begin{pmatrix} \boldsymbol{r}(t_f) - \boldsymbol{r}^*(t_f) \\ \boldsymbol{v}(t_f) - \boldsymbol{v}^*(t_f) \\ \boldsymbol{r}(t_0) - \bar{\boldsymbol{r}}(t_0) \\ \boldsymbol{v}(t_0) - \bar{\boldsymbol{v}}(t_0) \end{pmatrix} \tag{8}$$

be the vector of constraints. Then, the approximated impulsive-to-finite-burn conversion problem is formally stated as a constrained minimization:

$$\min_{\boldsymbol{s}} J(\boldsymbol{s}) \quad s.t. \quad \boldsymbol{l}(\boldsymbol{s}) = \boldsymbol{0}. \tag{9}$$

In Eq. (7), k is a scaling parameter that weighs the importance of the finite burn duration with respect to the constraints satisfaction. (In this work we set to $k = 0.01$.) Since the azimuth and elevation profiles for the thrust are assigned a priori, this problem formulation leads by definition to a sub-optimal solution. The minimization is solved with a standard NLP method, by employing an active-set algorithm and explicit numerical integration. Integrations are performed in a 2.9 GHz Intel Core i7 Unix machine where a $7^{\text{th}}/8^{\text{th}}$ order variable step Runge–Kutta–Fehlberg scheme is implemented within a Matlab mex file, with absolute and relative error tolerances equal to 2.5×10^{-14}.

2.2. Initial estimate of decision variables

An estimate of the decision variables is provided automatically and is only function of the impulsive maneuver. This estimate is used as initial guess for the direct minimization of Problem 2. The FBM conversion uses all of

the information available from the impulsive maneuver to estimate t_0 and t_f, along with the starting values of $\{a_j, b_j\}$. The result is a partially automated method that generates a time sub-optimal finite burn solution without the need to explicitly provide estimates for the start and end times, the starting values of the thrust direction angles, and their time derivatives.

2.2.1. Switching epochs estimate

For constant thrust, the mass equation (last one of Eq. (1)) can be solved analytically, and it is used to predict a burn time,

$$\Delta t = \frac{c_e \Delta m}{T_{\max}}, \tag{10}$$

where Δm is the mass consumption of the impulsive maneuver, according to Eq. (2). Estimates of t_0 and t_f are such that the maneuver epoch, t_i, is the midpoint of the finite burn arc,

$$t_0 = t_i - \frac{\Delta t}{2}, \qquad\qquad t_f = t_i + \frac{\Delta t}{2}. \tag{11}$$

2.2.2. Thrust angles estimate

The estimate for the thrust azimuth and elevation relies on the assumption that the thrust direction vector and its first and second time derivatives, $\boldsymbol{\gamma}, \dot{\boldsymbol{\gamma}}, \ddot{\boldsymbol{\gamma}}$, are equivalent to the impulsive maneuver direction and its first and second time derivatives at t_i, i. e.,

$$\begin{aligned}
\boldsymbol{\gamma}(t_i) &= \frac{\Delta \boldsymbol{v}}{\|\Delta \boldsymbol{v}\|}, \\
\dot{\boldsymbol{\gamma}}(t_i) &= \frac{\Delta \dot{\boldsymbol{v}}}{\|\Delta \boldsymbol{v}\|} - \frac{\Delta \boldsymbol{v} \cdot \Delta \dot{\boldsymbol{v}}}{\|\Delta \boldsymbol{v}\|^3} \Delta \boldsymbol{v}, \\
\ddot{\boldsymbol{\gamma}}(t_i) &= \left(3 \frac{(\Delta \boldsymbol{v} \cdot \Delta \dot{\boldsymbol{v}})^2}{\|\Delta \boldsymbol{v}\|^5} - \frac{\|\Delta \dot{\boldsymbol{v}}\|^2 + \Delta \boldsymbol{v} \cdot \Delta \ddot{\boldsymbol{v}}}{\|\Delta \boldsymbol{v}\|^3} \right) \Delta \boldsymbol{v} - 2 \frac{\Delta \boldsymbol{v} \cdot \Delta \dot{\boldsymbol{v}}}{\|\Delta \boldsymbol{v}\|^3} \Delta \dot{\boldsymbol{v}} + \frac{\Delta \ddot{\boldsymbol{v}}}{\|\Delta \boldsymbol{v}\|},
\end{aligned} \tag{12}$$

where

$$\Delta \dot{\boldsymbol{v}} := \boldsymbol{g}(\boldsymbol{r}, \boldsymbol{v}^+, t_i) - \boldsymbol{g}(\boldsymbol{r}, \boldsymbol{v}^-, t_i), \qquad \Delta \ddot{\boldsymbol{v}} := G_r \Delta \boldsymbol{v} + G_v \Delta \boldsymbol{g}, \tag{13}$$

and $G_r = [\partial \boldsymbol{g} / \partial \boldsymbol{r}]$, $G_v = [\partial \boldsymbol{g} / \partial \boldsymbol{v}]$ are the matrix of partial derivatives of the dynamics right-hand side. Cosine direction vector and its constituent angles

respect a well known, explicit, and unique relationship:

$$\begin{aligned}
\alpha(t_i) &= \tan^{-1}\frac{\gamma_y}{\gamma_x}, \qquad \dot{\alpha}(t_i) = \frac{\gamma_x\dot{\gamma}_y - \gamma_y\dot{\gamma}_x}{\gamma_x^2+\gamma_y^2},\\
\ddot{\alpha}(t_i) &= \frac{\gamma_x\ddot{\gamma}_y - \gamma_y\ddot{\gamma}_x}{\gamma_x^2+\gamma_y^2} - 2\frac{(\gamma_x\dot{\gamma}_x+\gamma_y\dot{\gamma}_y)(\gamma_x\dot{\gamma}_y-\gamma_y\dot{\gamma}_x)}{(\gamma_x^2+\gamma_y^2)^2},\\
\beta(t_i) &= \tan^{-1}\frac{\gamma_z}{\sqrt{\gamma_x^2+\gamma_y^2}}, \qquad \dot{\beta}(t_i) = \frac{\dot{\gamma}_z}{\sqrt{\gamma_x^2+\gamma_y^2}},\\
\ddot{\beta}(t_i) &= \frac{\ddot{\gamma}_z}{\sqrt{\gamma_x^2+\gamma_y^2}} - \frac{(\gamma_x\dot{\gamma}_x+\gamma_y\dot{\gamma}_y)\dot{\gamma}_z}{(\gamma_x^2+\gamma_y^2)^{3/2}},
\end{aligned} \tag{14}$$

where $\gamma_x, \gamma_y, \gamma_z$ indicate the components of $\boldsymbol{\gamma}$ at t_i along x, y, z, respectively. The same applies for its first and second time derivatives.

By comparing the thrust angles of Eqs. (14) with the approximated angle profiles in Eq. (5) (whose time derivatives are of straightforward computation), it is easy to compute the initial estimates for the first 6 coefficients of the cubic polynomials:

$$a_0 = \alpha(t_i), \quad a_1 = \dot{\alpha}(t_i), \quad a_2 = \ddot{\alpha}(t_i) \quad b_0 = \beta(t_i), \quad b_1 = \dot{\beta}(t_i), \quad b_2 = \ddot{\beta}(t_i). \tag{15}$$

The remaining coefficients for the cubic part are initially set to unity, i. e., $a_3 = b_3 = 1$, to trigger the cubic behavior in the sub-optimal solution. The direct

Algorithm 1 Direct to finite burn maneuver conversion.

Require: Specify dynamical model ▷ See Eq. (1)
  procedure FBM($\Delta\boldsymbol{v}, t_i, m^-$)
    Estimate engine switch epochs ▷ See Eqs. (10)–(11)
    Compute thrust directions $\{\boldsymbol{\gamma}(t_i), \dot{\boldsymbol{\gamma}}(t_i), \ddot{\boldsymbol{\gamma}}(t_i)\}$ ▷ See Eqs. (12)–(13)
    Compute thrust angles $\{\alpha, \dot{\alpha}, \ddot{\alpha}, \beta, \dot{\beta}, \ddot{\beta}\}$ ▷ See Eq. (14)
    Estimate quadratic coefficients $\{a_0, a_1, a_2, b_0, b_1, b_2\}$ ▷ See Eq. (15)
    Assign cubic coefficients to unity, $a_3 = b_3 = 1$
    Solve minimization Problem 2 ▷ See Eq. (9)
    if Convergence is attained **then**
      Save optimal decision variables in $\boldsymbol{y}^*$
    else
      Mark impulsive maneuver as unfeasible
    end if
  end procedure

optimization of a finite burn maneuver from a single known impulsive maneuver is described in Algorithm 1. Note that the impulsive-to-finite-burn maneuver conversion does not constrain the rate of change of the thrust pointing angles. This means that the angular rates, output of Algorithm 1, must be later assessed for compliance with the capabilities of the LISA Pathfinder attitude subsystem.

3. Navigation analysis

A navigation analysis is necessary to assess the feasibility of saddle point transfers in a high-fidelity simulated scenario. For this purpose, a navigation tool is specifically developed and implemented. Referring to Figure 3, the navigation analysis is composed by a preliminary assessment and a navigation assessment.

3.1. Preliminary assessment

The preliminary assessment performs a static analysis of transfers to the Sun–Earth gravitational saddle point. Considering radiometric observations (i. e., range and range rate) from a generic ground station (GS) on Earth, we lay out the main requirements on the transfer geometry. A sensitivity analysis is then performed to assess the transfer robustness against errors in the maneuvers profile. Ultimately, visibility windows are evaluated. The aim of the preliminary assessment is to prune out those transfers that are not compliant with static requirements on navigation, while also providing comprehensive geometrical information on the remaining transfers. The information is then used for dynamical analyses, e. g., orbit determination.

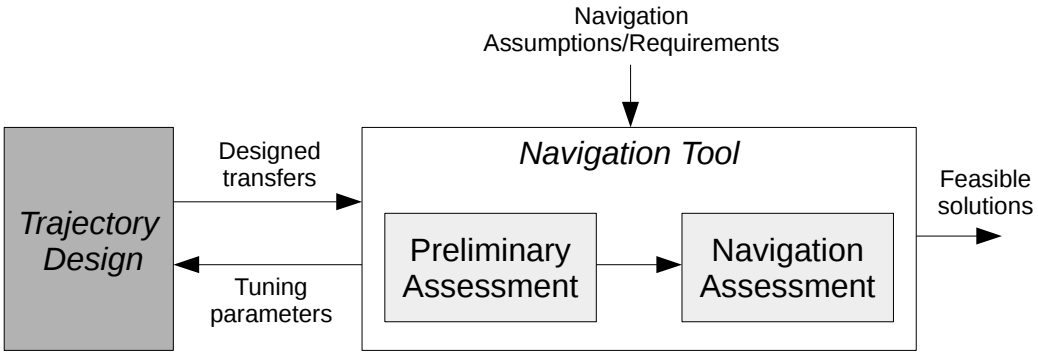

Figure 3: Architecture of navigation tool.

3.1.1. Relative geometry evaluation

Several geometrical configurations are investigated in order to identify potential hazardous conditions for the spacecraft. Let $\boldsymbol{R}$, $\boldsymbol{R}_M$ $\boldsymbol{R}_S$, and $\boldsymbol{R}_{\text{gs}}$ be the spacecraft, Moon, Sun, and ground station position vectors with respect to the Earth center, respectively. Then, the spacecraft range vector to the ground station is $\boldsymbol{\rho} = \boldsymbol{R} - \boldsymbol{R}_{\text{gs}}$, the Sun-Spacecraft-Earth angle is ψ, the exclusion angle is ϕ, and the spacecraft elevation angle with respect to the ground station is El. The geometry of the spacecraft transfer in the Sun–Earth–Moon system is illustrated in Figure 4, where the relevant geometric quantities are highlighted. Note that the exclusion angle is approximated as the Sun-Earth-Spacecraft angle in this work, as opposed to the Sun-GS-Spacecraft. The approximation holds valid in deep-space transfers, i. e., when $\|\boldsymbol{R}\| \gg \|\boldsymbol{R}_{\text{gs}}\|$.

Table 1 summarizes the main requirements on relevant geometrical parameters. The Spacecraft-to-Earth distance is constrained to prevent transfers involving very large distances, which may trigger issues for communications, and the Spacecraft-to-Earth/Moon distances are constrained to avoid close encounters with either celestial bodies. The minimum distance with respect to either Earth or Moon is equal to $10,000$ km, while the spacecraft cannot go further than 2 million km from the Earth.

Generally, in long transfers eclipses due to Moon and/or Earth and Moon occultations may occur. Depth and duration of each eclipse mainly depend

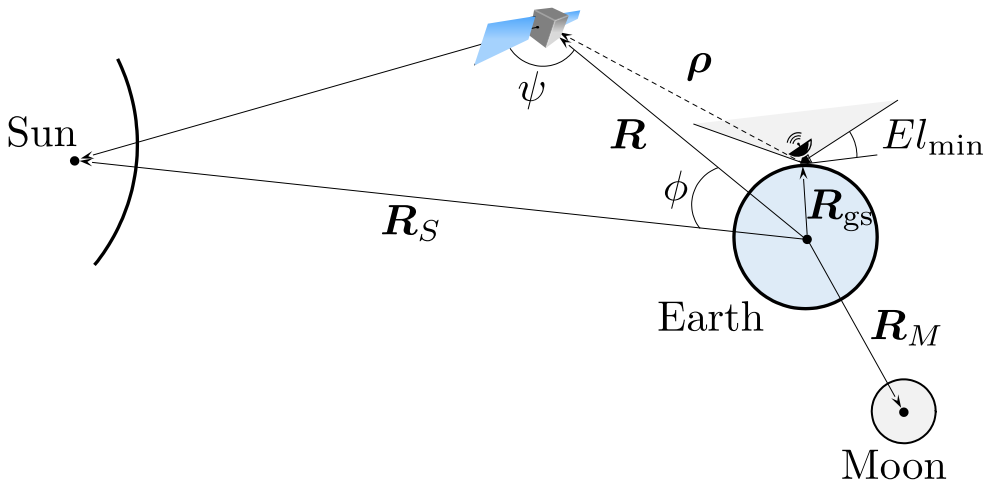

Figure 4: Geometry of the tracking problem.

Table 1: Requirements on relative geometry.

Parameter	Requirement
Earth distance	$\|\boldsymbol{R}\| \in [10^4, 2 \times 10^6]$ km
Spacecraft-Moon range	$\|\boldsymbol{R}_M - \boldsymbol{R}\| > 10^4$ km
Earth/Moon eclipses	To be avoided when possible
Moon occultations	To be avoided when possible
Solar conjunctions	$\phi > 0.5$ deg
GS visibility	$El > El_{\min} = 10$ deg
Antenna pointing angle	$\psi \in [0, \pi]$ rad

on the trajectory and are typically difficult to predict, although a lower distance from the ecliptic plane, and thus to the Moon orbit plane, increases the probability of eclipse occurrences. In this work, transfers with long and deep eclipses are penalized because they may pose severe restrictions to the spacecraft operability. On the other hand, prolonged occultation duration causes interferences in the probe-to-ground stations communication link, which can limit the number or affect the quality of radiometric measurements.

Solar conjunctions are expected to occur close to SP passages, where the exclusion angle approaches zero. A requirement is placed on solar conjunctions to limit the amount of deteriorated radiometric data which in turn may degrade the spacecraft knowledge accuracy (Yarnoz et al., 2006). Referring to Figure 4, the exclusion angle is thus constrained to be $\phi > 0.5$ deg.

The elevation angle profile with respect to one or multiple ground stations identifies the trajectory portions where the GS sensor mounting constraints are satisfied and the spacecraft is in visible conditions. The requirement for visibility is a minimum elevation above the horizon in the ground station topocentric frame, i. e., $El > El_{\min}$. Typically, $El_{\min}$ depends on the specific ground station characteristics. In this work, a conservative value of $El_{\min} = 10$ deg is used for all GS.

The Sun-Spacecraft-Earth angle (ψ in Figure 4) profile may be directly related to the antenna pointing effort if the antenna is gimbaled, or the antenna misalignment if the antenna is rigidly attached to the spacecraft. To avoid large deviations from the nominal antenna pointing angle, thus limiting the need of large attitude control maneuvers, the Sun-Spacecraft-

Earth angle shall be bounded in $\psi_{\min} < \psi < \psi_{\max}$, where $\psi_{\min}$ and $\psi_{\max}$ depend on the probe specific structural configuration.

3.1.2. Solution robustness

Due to the nonlinearity of the vector field and the severe requirements on the SP passage (Hees et al., 2016; Galianni et al., 2012; Bekenstein and Magueijo, 2006; Topputo et al., 2018b), even small errors can jeopardize the designed transfer and eventually undermine the probability of an encounter with the SP. Therefore, an analysis of the solution sensitivity to maneuvering errors is of paramount importance for the identification and pruning of those transfers characterized by high sensitivity, for which large control efforts would likely be required.

Monte Carlo analyses are performed by propagating the nominal initial conditions with a set of noisy control profiles with uncertainties on magnitude, direction, duration, and timing of the nominal finite burn maneuvers. The resulting samples statistics provides quantitative information on the saddle point reachability. This process is intended as a design sensitivity analysis, and the effects of errors due to other processes, such as the measurement acquisition process, orbit determination process, etc., are not considered.

3.1.3. Visibility windows

Coverage, or visibility, windows depend on the observed object trajectory and on the ground station characteristics (e. g., geographical coordinates, mounting mechanism). A coverage window is assumed here as an un-thrusted portion of the trajectory, not affected by solar conjunctions nor Moon occultations, and in which both elevation and pointing constraints of the ground station are satisfied.

Let Δt_c be the coverage duration, i. e., the time interval in which the spacecraft is visible from the selected GS, and let Δt_s be the temporal separation between two consecutive coverage windows. In this work, a coverage window is identified when the coverage duration is between $\Delta t_{c_{\min}} = 3$ hours (to avoid having too short windows) and $\Delta t_{c_{\max}} = 8$ hours (to limit ground operation costs). Multiple coverage windows in a short duration neither reflects operative conditions where the selected ground station could be unavailable for scheduling reasons or technical problems nor typically leads to significant improvements in the orbit knowledge (Bowell et al., 2002). Thus, temporally close windows with $\Delta t_s < 7$ days are also discarded.

Additional criteria are not considered here and may be added to simulate the existence of other operative constraints, e. g., simultaneous radiometric measurements from multiple GS shall be minimized to avoid data overlapping. Once one or multiple ground stations are selected, information on coverage window is then used to generate the radiometric data and ultimately simulate the estimation process.

3.2. Navigation assessment

The navigation assessment is devoted to the simulation of the radiometric data acquisition process, the computation, through a covariance analysis, of the achievable state knowledge, and the estimation of the required correction maneuvers.

3.2.1. Measurement model

The equations of motion and the measurement model provide the basic framework for describing the motion of a satellite with respect to a ground station. Observation data is expressed as

$$\boldsymbol{z} = \boldsymbol{h}(\boldsymbol{P}, \boldsymbol{X}, \boldsymbol{C}) + \boldsymbol{\epsilon}, \tag{16}$$

where $\boldsymbol{z} = (z_1, \ldots, z_n)$ denotes a n-dimensional vector of measurements performed at times $t_1, \ldots, t_n$, $\boldsymbol{h}$ is the numerical model for the observations as function of the vector of processes $\boldsymbol{P}$, the state $\boldsymbol{X}$ at epoch t (see Eq. (1)), and the vector of considered parameters $\boldsymbol{C}$; $\boldsymbol{\epsilon} \sim (0, I)$ is a zero-mean randomly distributed vector that accounts for the difference between actual and modeled observations due to measurements error (Montenbruck and Gill, 2000). The vector $\boldsymbol{C}$ comprises parameters that are supposed to be uncertain but are not adjusted as part of the estimation process. The vector $\boldsymbol{\epsilon}$ includes effects due to Earth orientation noises, clock instabilities, signal delays due to transmission media, thermal noises, and it is prewhitened to have unit covariance matrix.

The practical solution of the orbit estimation problem is complicated by the fact that $\boldsymbol{h}$ is a highly nonlinear function of its arguments. The measurement model is then used in its simplified first-order Taylor expansion around a reference $(\boldsymbol{P}, \boldsymbol{X}, \boldsymbol{C})^{\text{ref}}$. Without loss of generality, we assume here that the processes and the consider parameters are small quantities with an expected value of zero, i. e., $\boldsymbol{P}^{\text{ref}} = \boldsymbol{0}$ and $\boldsymbol{C}^{\text{ref}} = \boldsymbol{0}$. Linearization of Eq. (16) yields

$$\boldsymbol{y} = H_p \boldsymbol{p} + H_x \boldsymbol{x} + H_c \boldsymbol{c} + \boldsymbol{\epsilon}, \tag{17}$$

where $\boldsymbol{y} = \boldsymbol{z} - \boldsymbol{h}(\boldsymbol{P}^{\text{ref}}, \boldsymbol{X}^{\text{ref}}, \boldsymbol{C}^{\text{ref}})$ denotes the difference between the actual observations and the observations predicted from the reference trajectory, lower-case Latin letters are the difference between the argument and the reference, $\boldsymbol{p} = \boldsymbol{P} - \boldsymbol{P}^{\text{ref}}$, $\boldsymbol{x} = \boldsymbol{X} - \boldsymbol{X}^{\text{ref}}$, and $\boldsymbol{c} = \boldsymbol{C} - \boldsymbol{C}^{\text{ref}}$, respectively, and $H_q = [\partial \boldsymbol{h}/\partial \boldsymbol{q}]|_{(\boldsymbol{P},\boldsymbol{X},\boldsymbol{C})^{\text{ref}}}$ with $\boldsymbol{q} = \{\boldsymbol{p}, \boldsymbol{x}, \boldsymbol{c}\}$ is the Jacobian of the measurement model with respect to its arguments. In the following, $\boldsymbol{q}$ will be used interchangeably for $\boldsymbol{p}$, $\boldsymbol{x}$, and $\boldsymbol{c}$.

Note that, in the absence of real telemetry data, the actual measurements in $\boldsymbol{z}$ are simulated and stored offline and later retrieved during the orbit estimation. Radiometric data for range and range-rate is simulated by defining two dedicated versions of measurement model,

$$\rho = \sqrt{\boldsymbol{\rho}^{\text{T}}\boldsymbol{\rho}}, \qquad \dot{\rho} = \frac{\boldsymbol{\rho}^{\text{T}}\boldsymbol{\eta}}{\rho}, \tag{18}$$

where ρ is the range measurement and $\dot{\rho}$ is the range-rate measurement, and $\boldsymbol{\eta} = \boldsymbol{V} - \boldsymbol{V}_{\text{gs}}$ is the relative velocity of the spacecraft with respect to the ground station. Table 2 reports the typical frequencies and errors achievable using current ground stations technologies.

Table 2: Range and Doppler measurements assumptions (Landgraf et al., 2014).

Parameter	Value
Range frequency	once per pass
Range noise (1σ)	20 m
Range bias	20 m
Doppler frequency	once every 10 min
Doppler noise (1σ)	0.03 mm/s
Doppler bias	0 mm/s

3.2.2. Error sources

Numerous effects are incorporated in the estimation process to compensate for differences between the numerical and actual environment, leading to a more realistic feasibility evaluation of the designed trajectories and a more conservative estimation of the state covariance matrix. Besides measurements errors, the estimation process is refined with the inclusion of a)

systematic/bias errors, through a consider covariance approach and b) correlated process noises, modeled as Gauss–Markov processes, also known as exponentially correlated random variables (ECRV). A Gauss–Markov process obeys Langevin differential equation (Tapley et al., 2004),

$$\dot{\xi}(t) = -\beta\xi(t) + w(t), \tag{19}$$

where $\xi(t)$ is the ECRV, $w(t)$ is zero-mean white Gaussian noise with variance σ^2, and $\beta = 1/\tau$, with τ as the correlation time.

The consider parameters vector includes ground station location biases, assumed equal to 30 cm in equatorial plane error and 1 m out of equatorial plane error, and systematic errors in the measurement modeling of range and range-rate e. g., due to system calibration errors (refer to Table 2). Thus, $\boldsymbol{C} \in \mathbb{R}^{(3*n_{gs}+2)\times 1}$, where n_{gs} is the number of ground station used to perform the observations. Table 3 shows the Gauss–Markov processes, $\boldsymbol{P} \in \mathbb{R}^{9\times 1}$, considered in this work.

Table 3: Gauss–Markov processes.

Noise source	Standard deviation, $\sqrt{\sigma^2}$	Correlation time, τ
Solar radiation pressure	10% of the nominal force along same direction	1 day
Thrust misalignment	1% in magnitude and 0.5 deg in pointing angles	1 day
Residual accelerations	10^{-11} km/s^2 in all directions	1 day

3.2.3. Orbit estimation

A covariance analysis is conducted to determine the achievable level of accuracy in the spacecraft position and velocity knowledge along the entire transfer (Modenini et al., 2017). In this paper, a square root information filter (SRIF) is adopted for the orbit determination (OD). The SRIF is preferred to other common filtering techniques, for instance extended and unscented Kalman filters, due to its numerical robustness (Montenbruck and Gill, 2000). The SRIF processes a single vector of measurements at a time and yields

sequential state estimates at the measurement times. The orbit estimation process consists of two main steps: the time update and the measurement update. The procedure of time and measurement updates is carried out until the desired number of observations is processed. Let P denote the covariance matrix of a random variable, then its inverse is the information matrix, $\Lambda = P^{-1}$. In the SRIF, the square root of the information matrix R is operated on for time and measurement updates, rather than the covariance matrix, where $P = R^{-1}R^{-\mathrm{T}}$ (Tapley et al., 2004).

The trajectory to be analyzed is split into a series of coast and propelled legs. Compatibly with the definition of visibility window given in Section 3.1.3, measurements can not be taken during engine operation and orbit estimation is only performed within the coast legs. Each coast leg is further divided into mapping intervals of 12 hours and the solution state and control are discretized to match the fix-step mapping time. The navigation assessment routine loops through the map intervals and sequentially checks if observations are available within the current map interval. In case observations are available, the square root information filter is applied after the measurements are retrieved and pseudo-measurement are generated based on the current state. In the time intervals when no observations are available, the estimated state and covariance are propagated forward with the discrete form of the equations of motion:

$$\begin{aligned} \boldsymbol{p}_{k+1} &= M_{k+1}\boldsymbol{p}_k + \boldsymbol{w}_k, \\ \boldsymbol{x}_{k+1} &= \Phi_{p_{k+1}}\boldsymbol{p}_k + \Phi_{x_{k+1}}\boldsymbol{x}_k + \Phi_{c_{k+1}}\boldsymbol{c}_k, \\ \boldsymbol{c}_{k+1} &= \boldsymbol{c}_k, \end{aligned} \tag{20}$$

where subscripts k and $k+1$ relate to quantities evaluated at discrete times t_k and t_{k+1}, respectively, $M_{k+1} = e^{(t_{k+1}-t_k)/\tau} I_9$ is the process transition matrix (solution of Eq. (19)), $\boldsymbol{w}_k$ is the process noise, $\Phi_{q_{k+1}}$ for $q = \{p, x, c\}$ is the state transition matrix mapping deviation in the argument q to the state $\boldsymbol{x}$ from epochs t_k to t_{k+1}. In this work, Φ_p is computed with a numerical quadrature at each step of the estimation process, Φ_x is retrieved by means of linear interpolation based on the state transition matrix of the reference trajectory (calculated offline by integrating the variational equations together with the main motion), and Φ_c is zero because the consider parameters only affects the measurement model and not the equations of motion. The process noise has mean $\bar{\boldsymbol{w}}$ and covariance $Q_w = Q_p(I_9 - M^{\mathrm{T}}M) = R_w^{-1}R_w^{-\mathrm{T}}$, where Q_p is the variance of the Gauss–Markov processes (see Table 3) defined in

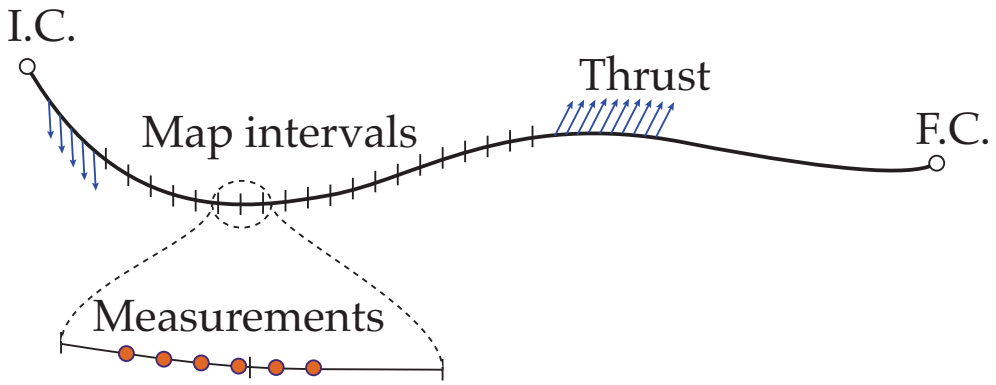

Figure 5: Layout of the trajectory subdivision for navigation assessment.

the reference frame where Eq. (20) is cast and I_9 is the identity matrix of dimension 9. Figure 5 highlights the coverage windows with respect to the division of the transfer into legs and mapping intervals, while the navigation assessment procedure is described in Algorithm 2.

Let $[R_p, \boldsymbol{b}_p]_k$, $[R_x, \boldsymbol{b}_x]_k$, and $[R_c, \boldsymbol{b}_c]_k$ be the a priori information arrays at time t_k for $\boldsymbol{p}$, $\boldsymbol{x}$, and $\boldsymbol{c}$, respectively, such that $\boldsymbol{b}_{q_k} = R_{q_k}\boldsymbol{q}_k$ with $\bar{\boldsymbol{q}}_k = \boldsymbol{q}_k + \boldsymbol{\chi}_{q_k}$, where $\boldsymbol{q}_k$ is the true value and $E\left[\boldsymbol{\chi}_{q_k}\right] = \boldsymbol{0}$, $E\left[\boldsymbol{\chi}_{q_k}\boldsymbol{\chi}_{q_k}^{\mathrm{T}}\right] = P_{q_k} = R_{q_k}^{-1}R_{q_k}^{-\mathrm{T}}$; then the covariance matrix for the processes, state, and consider parameters read

$$P_k = \begin{bmatrix} P_p & 0 & SP_c \\ 0 & P_x & \\ (SP_c)^{\mathrm{T}} & & P_c \end{bmatrix}_k = R_k^{-1}R_k^{-\mathrm{T}}, \quad \text{with} \quad R_k = \begin{bmatrix} R_x & R_{px}^{\mathrm{T}} & R_{xc} \\ R_{px} & R_p & R_{pc} \\ R_{pc}^{\mathrm{T}} & R_{pc}^{\mathrm{T}} & R_c \end{bmatrix}_k, \tag{21}$$

where $S_k = [\partial\boldsymbol{x}/\partial\boldsymbol{c}]_k$ is the sensitivity matrix and $P_c = \boldsymbol{c}^{\mathrm{T}}\boldsymbol{c}$ is the diagonal covariance matrix of the consider parameters. Note that due the dynamics of $\boldsymbol{c}_{k+1}$, P_c is also constant. Assume also that at time t_k an observation is made such that

$$\boldsymbol{y}_k = \begin{bmatrix} H_p & H_x & H_c \end{bmatrix}_k \begin{pmatrix} \boldsymbol{p} \\ \boldsymbol{x} \\ \boldsymbol{c} \end{pmatrix}_k + \boldsymbol{\epsilon}_k. \tag{22}$$

Then, the SRIF time update for the arguments $\boldsymbol{p}$, $\boldsymbol{x}$, and $\boldsymbol{c}$ is given by

$$\begin{bmatrix} R_p^* & R_{pp}^* & R_{px}^* & R_{pc}^* \\ 0 & \bar{R}_p & \bar{R}_{px} & \bar{R}_{pc} \\ 0 & 0 & \bar{R}_x & \bar{R}_{xc} \\ 0 & 0 & 0 & \bar{R}_c \end{bmatrix}_{k+1} \begin{pmatrix} \boldsymbol{p}_k \\ \boldsymbol{p}_{k+1} \\ \boldsymbol{x}_{k+1} \\ \boldsymbol{c}_{k+1} \end{pmatrix} = \begin{pmatrix} \boldsymbol{b}_p^* \\ \bar{\boldsymbol{b}}_p \\ \bar{\boldsymbol{b}}_x \\ \bar{\boldsymbol{b}}_c \end{pmatrix}_{k+1}, \tag{23}$$

Algorithm 2 Navigation assessment algorithm.

Require: ULTIMAT, SPICE, guidance and preliminary assessment candidate solution ν

procedure NAVIGATION ASSESSMENT(ν)
    Define navigation settings
    Load object parameters
    Load ground station parameters
    Generate measurement time stamp for each GS
    Nondimensionalize quantities
    function INITIALIZATION
        Initialize the number of states, processes, and consider parameters
        Initialize the sensitivity matrix
        Assign the consider parameters covariance
        Build the a priori covariance matrix
        Assign the measurement noise matrix
    end function
    function ESTIMATION
        Find trajectory legs, defined between low thrust arcs and coast arcs
        Retrieve initial conditions for candidate solution from SPICE kernel, $\boldsymbol{x}_0$
        for $i \leftarrow 1, n_L$ **do** ▷ Loop through n_L trajectory legs
            Discretize solution to match fix-step mapping time
            for $k \leftarrow 1, n_M$ **do** ▷ Loop through n_M map points within ith leg
                if $\exists$ measurement in $[t_k, t_{k+1}]$ **then**
                    Retrieve observations data of reference
                    Generate the pseudo-measurement
                    Apply square root information filter ▷ See Algorithm 3
                    Get filter estimates and covariance at current time t_i
                    Store SRIF output for post-processing
                end if
                if $t_i \neq t_{k+1}$ **then**
                    Propagate state and covariance until end of current map interval
                    Update initial conditions for next map interval
                end if
            end for (k)
        end for (i)
        Save and post-process estimation results for candidate solution ν
    end function
end procedure

where the time update of the information array (indicated with barred quantities in Eq. (23)) is computed by applying a series of orthogonal Givens

transformation (Givens, 1958) such that

$$\bar{T}_k \begin{bmatrix} -R_w M_{k+1} & R_w & 0 & 0 & \mathbf{0} \\ R_p - R_{px}\Phi^{-1}_{x_{k+1}}\Phi_{p_{k+1}} & 0 & R_{px}\Phi^{-1}_{x_{k+1}} & R_{pc} & \boldsymbol{b}_p \\ -R_x\Phi^{-1}_{x_{k+1}}\Phi_{p_{k+1}} & 0 & R_x\Phi^{-1}_{x_{k+1}} & R_{xc} & \boldsymbol{b}_x \\ 0 & 0 & 0 & R_c & \boldsymbol{b}_c \end{bmatrix}_k = \begin{bmatrix} R^*_p & R^*_{pp} & R^*_{px} & R^*_{pc} & \boldsymbol{b}^*_p \\ 0 & \bar{R}_p & \bar{R}_{px} & \bar{R}_{pc} & \bar{\boldsymbol{b}}_p \\ 0 & 0 & \bar{R}_x & \bar{R}_{xc} & \bar{\boldsymbol{b}}_x \\ 0 & 0 & 0 & \bar{R}_c & \bar{\boldsymbol{b}}_c \end{bmatrix}_{k+1}, \tag{24}$$

and $\bar{T}_k$ is the Givens transformation matrix that upper triangularize the information matrix. Starred quantities that are generated as part of the time update are typically used for smoothing (Tapley et al., 2004) and are not used in this paper. Similarly, the SRIF measurement update is the solution of

$$\begin{bmatrix} R_p & R_{px} & R_{pc} \\ 0 & R_x & R_{xc} \\ 0 & 0 & R_c \end{bmatrix}_{k+1} \begin{pmatrix} \boldsymbol{p} \\ \boldsymbol{x} \\ \boldsymbol{c} \end{pmatrix}_{k+1} = \begin{pmatrix} \boldsymbol{b}_p \\ \boldsymbol{b}_x \\ \boldsymbol{b}_c \end{pmatrix}_{k+1}, \tag{25}$$

where the measurement update of the information matrix is computed by applying a series of orthogonal Givens transformation (Givens, 1958) such that

$$T_k \begin{bmatrix} \bar{R}_p & \bar{R}_{px} & \bar{R}_{pc} & \bar{\boldsymbol{b}}_p \\ 0 & \bar{R}_x & \bar{R}_{xc} & \bar{\boldsymbol{b}}_x \\ 0 & 0 & \bar{R}_c & \bar{\boldsymbol{b}}_c \\ H_p & H_x & H_c & \boldsymbol{y} \end{bmatrix}_k = \begin{bmatrix} R_p & R_{px} & R_{pc} & \boldsymbol{b}_p \\ 0 & R_x & R_{xc} & \boldsymbol{b}_x \\ 0 & 0 & R_c & \boldsymbol{b}_c \\ 0 & 0 & 0 & \boldsymbol{e} \end{bmatrix}_k, \tag{26}$$

T_k is the Givens transformation matrix that upper triangularize the information matrix, and $\boldsymbol{e}$ is the vector of residuals. Eqs. (23)–(26) are sequentially applied until the desired number of observations is processed, where the information arrays and variables updates from the measurement update step are used in the next time update step. The SRIF is described in Algorithm 3. After the time and measurement updates, the state and covariance estimates yield:

$$\begin{aligned} \boldsymbol{X}_{\text{est}} &= \boldsymbol{X} + \boldsymbol{x}, \\ P^{(\text{as})}_{\text{est}} &= P^{(\text{as})} + SP_cS^{\text{T}}, \end{aligned} \tag{27}$$

where $\boldsymbol{X}_{\text{est}}$ is the estimate of the state, $P^{(\text{as})}_{\text{est}}$ is the estimate of the covariance matrix of the augmented state, i. e., including both process and state but not the consider parameters, $\boldsymbol{x}$ is found with back substitution on Eq. (25) and the measurement update of the sensitivity matrix is

$$S = -\begin{bmatrix} R_x & 0 \\ R_{px} & R_p \end{bmatrix}^{-1} \begin{bmatrix} R_{xc} \\ R_{pc} \end{bmatrix}. \tag{28}$$

Algorithm 3 Square root information filter algorithm.

function SRIF($t, \boldsymbol{X}, \boldsymbol{C}, P, S$)
  Compute square root information matrix ▷ See Eq. (21)
  Compute information arrays $[\bar{R}_p, \bar{\boldsymbol{b}}_p]$, $[\bar{R}_x, \bar{\boldsymbol{b}}_x]$, and $[\bar{R}_p, \bar{\boldsymbol{b}}_c]$
  for $j \leftarrow 1, n_O$ **do** ▷ Loop through number of observations, n_O
    Retrieve Φ_x from current to measurement epoch by interpolation
    Compute Φ_p with a numerical quadrature
    Retrieve process noise and covariance Q_w
    Retrieve the reference pseudo-measurement and generate a current observation
    Compute Jacobian of measurement model with central finite difference scheme
    Pre-whiten the measurement with factorization of the noise covariance
    Perform the SRIF time update ▷ See Eqs. (23)–(24)
    Perform the SRIF measurement update ▷ See Eqs. (25)–(26)
    Compute the state and covariance estimates ▷ See Eq. (27)
    Update current time for next iteration
  end for (j)
end function

3.2.4. Saddle point passage confidence

Given the 1σ knowledge at the SP passage epoch, the 95% confidence ellipsoid associated with the position uncertainty of the satellite is recovered using principal axes decomposition and exploiting the fact that the sum of squared Gaussian variables is distributed according to the chi-square distribution. Then, a final evaluation of the intersection area between the confidence ellipsoid and the spherical tolerance volume around the SP allows determining whether the spacecraft flies by the SP region with the required level of confidence.

3.2.5. Estimation of correction maneuvers

The overall navigation cost, necessary to keep the spacecraft on the nominal path, is estimated through the selection of a dedicated guidance and/or control strategy. Closed-loop control laws trigger maneuvers to track the reference guidance, whereas closed-loop guidance laws trigger maneuvers that globally updates the spacecraft trajectory to meet mission requirements and target state. Maneuvers are computed either when the state knowledge exceeds a certain threshold, or at prescribed time stamps (for example defined by the flight dynamics team on ground). Many control/guidance laws exist based, for instance, on the control of the full state vector, the velocity components, or just the unstable components (Bryson, 1975), linearization around reference path, applications of generalized Zero-Effort-Miss/Zero-

Effort-Velocity feedback guidance (Guo et al., 2013), etc.

A commonly used guidance method for interplanetary navigation is the differential guidance (Crassidis and Markley, 2003; Park and Scheeres, 2006). This formulation is based on the idea of using two impulsive maneuvers to cancel both the final position and velocity deviations. To the first-order approximation, deviations from the nominal state can be propagated with the state transition matrix (STM),

$$\begin{pmatrix} \delta\boldsymbol{r}_{j+1} \\ \delta\boldsymbol{v}_{j+1} \end{pmatrix} = \begin{bmatrix} \Phi_{rr} & \Phi_{rv} \\ \Phi_{vr} & \Phi_{vv} \end{bmatrix} \left\{ \begin{pmatrix} \delta\boldsymbol{r}_{j} \\ \delta\boldsymbol{v}_{j} \end{pmatrix} + \begin{pmatrix} \mathbf{0} \\ \Delta\boldsymbol{v}_{j} \end{pmatrix} \right\} + \begin{pmatrix} \mathbf{0} \\ \Delta\boldsymbol{v}_{j+1} \end{pmatrix}, \quad (29)$$

where subscripts correlate to epoch, $\delta\boldsymbol{r}$ and $\delta\boldsymbol{v}$ are the position and velocity deviation, respectively, Φ_{rr}, Φ_{rv}, Φ_{vr}, and Φ_{vv} are the 3-by-3 blocks of $\Phi(t_j, t_{j+1})$, that is the STM from t_j to t_{j+1} associated to the nominal solution, and $\Delta\boldsymbol{v}_j$ and $\Delta\boldsymbol{v}_{j+1}$ are the navigation correction maneuvers at epoch t_j and t_{j+1}. The linear system in Eq. (29) can be solved explicitly once the STM matrix is available. However, the second $\Delta\boldsymbol{v}_{j+1}$ is usually not applied in practice, since at the time of arrival at the final point a new maneuver can be calculated in a receding horizon approach. Based on this, the approach can be slightly modified including only one maneuver, which is obtained from the minimization of the deviations from the nominal state in a least square residuals sense. Eq. (29) is altered as

$$\begin{pmatrix} \delta\boldsymbol{r}_{j+1} \\ \delta\boldsymbol{v}_{j+1} \end{pmatrix} = \begin{bmatrix} \Phi_{rr} & \Phi_{rv} \\ \Phi_{vr} & \Phi_{vv} \end{bmatrix} \left\{ \begin{pmatrix} \delta\boldsymbol{r}_{j} \\ \delta\boldsymbol{v}_{j} \end{pmatrix} + \begin{pmatrix} \mathbf{0} \\ \Delta\boldsymbol{v}_{j} \end{pmatrix} \right\}, \quad (30)$$

Then, the correction maneuver $\Delta\boldsymbol{v}_j$ is determined such that the magnitude of the perturbation at time t_{j+1} is minimum, i. e.,

$$J = ||\delta\boldsymbol{r}_{j+1}||^2 + q||\delta\boldsymbol{v}_{j+1}||^2, \quad (31)$$

where q adjusts dimensions. A straightforward application of variations analysis to Eq. (31) leads to

$$\Delta\boldsymbol{v}_j = -\left(\Phi_{rv}^{\mathrm{T}}\Phi_{rv} + q\Phi_{vv}^{\mathrm{T}}\Phi_{vv}\right)^{-1}\left(\Phi_{rv}^{\mathrm{T}}\Phi_{rr} + q\Phi_{vv}^{\mathrm{T}}\Phi_{vr}\right)\delta\boldsymbol{r}_j - \delta\boldsymbol{v}_j. \quad (32)$$

The control law in Eq. (32) is applied whenever OD is performed. A latency interval of 2 days is considered between the epoch of the last measurement update within a coverage window and the application of the correction maneuvers to ensure enough time for flight dynamics operations and a couple

of uplink opportunities. The described process is repeated at intermediate points until the end of the trajectory is reached.

A Monte Carlo simulation is set up to evaluate the total Δv required, for different levels of confidence. In particular, starting from an initial distribution with mean μ_0 and covariance P_0, a set of samples $\boldsymbol{x}_0^i$ is generated. The samples are propagated forward, up to the first correction epoch t_1, where the maneuver $\Delta\boldsymbol{v}_1$ is determined with Eq. (32). The procedure is repeated until the end of the transfer. The estimation of the total navigation cost is then obtained as the sum of all maneuvers, $\Delta v = \sum_{j=1}^{N} \|\Delta\boldsymbol{v}_j\|$.

Some assumptions for the computation and implementation of trajectory correction maneuvers (TCM) are implicitly introduced, which is worth clarifying. The TCM are derived from the reference trajectories rather than from the reconstructed ones, which means the OD process is not considered in the loop. Nonetheless, for a well-behaved OD process, the distance between estimated and deviated trajectories is bounded. Furthermore, TCM are modeled in terms of $\Delta\boldsymbol{v}_j$, even if they have to be performed using the finite-thrust propulsion system available on board. This error is recovered a posteriori by re-evaluating the feasibility of the TCM with finite thrust durations (computed using actual spacecraft mass and thrust levels at t_j). Finally, TCM are assumed free of uncertainties. Numerical simulations resulted in maneuvers with very small magnitude, and their uncertainties can be thus neglected in first approximation. The decrease in accuracy and optimality of a linear control approach, when compared to more detailed closed-loop control laws, is motivated by the better numerical efficiency in terms of computational speed. The method presented here to compute the navigation cost yields an estimation of the actual cost needed to fly a pre-computed trajectory. Despite the high-fidelity nature of the present analysis, a slight variation of this cost is expected when using real-world telemetry data.

4. Finite burn optimal transfers to the saddle point

4.1. Saddle point fly-throughs from Sun–Earth libration point orbits

The finite burn maneuver conversion, as described in Algorithm 1, is applied to trajectories from the Sun–Earth $L_{1,2}$ LPO regions to the gravitational saddle point. The trajectories feature five successive impulsive maneuvers designed in the high-fidelity roto-pulsating restricted n-body problem (RPRnBP); see Dei Tos and Topputo (2019) for details. Out of the 393 (from L_1) and 191 (from L_2) SP optimal impulsive solutions taken from

Table 4: Solution parameters for sample finite burn transfer to SP in the RPRnBP. Here, h_{LGA} stands for altitude of lunar closest passage (counted if less than $70,000$ km), and t_{LT} is the total duration of the low-thrust burn.

Figure	Δv [m/s]	ToF [days]	h_{LGA} [km]	t_{LT} [days]	Δm [kg]
Figure 6a	0.99	239.5	—	5.73	0.84
Figure 6b	0.26	188.1	—	1.50	0.22
Figure 6c	0.30	172.7	—	1.72	0.25
Figure 6d	1.34	129.9	40030	7.73	1.13
Figure 7a	0.09	183.1	—	0.50	0.07
Figure 7b	0.14	122.5	15731	0.83	0.12
Figure 7c	3.53	102.0	—	20.4	3.00
Figure 7d	10.3	1002.5	—	62.1	9.27
Figure 8a	1.62	323.9	62111	9.30	1.40
Figure 8b	1.07	111.1	—	7.30	1.10
Figure 8c	0.72	537.8	—	4.20	0.60
Figure 8d	0.71	173.3	15601	4.10	0.59
Figure 9a	0.03	267.1	19498	0.16	0.02
Figure 9b	0.61	319.6	—	3.50	0.50
Figure 9c	8.48	102.4	—	49.3	7.20
Figure 9d	3.77	1011.9	—	22.1	3.20

Topputo et al. (2018c), 82% and 58% prove feasible when the impulsive maneuvers are spread into finite burn arcs. Sample trajectories departing from L_1 and L_2 are shown in Figures 6–7 and Figures 8–9, respectively. The solutions are grouped into families and only representative transfers for each family are displayed here for clarity. Table 4 shows the parameters for the solutions shown. Few important observations arise:

1. There exists a lower bound for the ToF, roughly equal to 102 days from both $L_{1,2}$ libration point orbit regions.

2. There are plenty of transfers to the SP with ultra-low deterministic Δv from the Sun–Earth LPO regions. Exploitation of the chaotic nature of the n-body problem enables a S/C orbiting in the $L_{1,2}$ neighborhood to reach the SP for as low Δv as few centimeters per second.

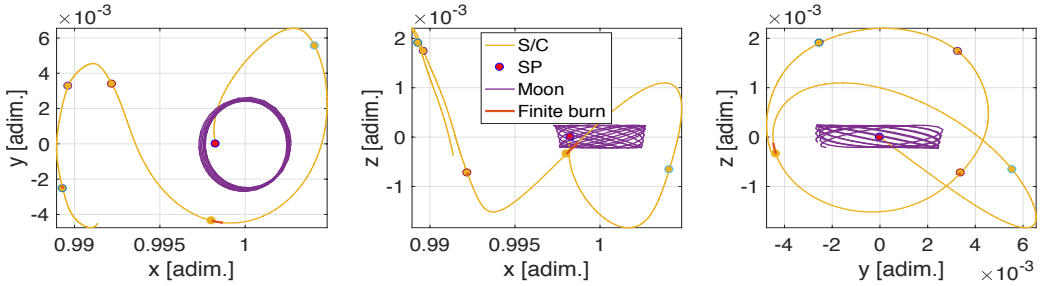

(a) Family δ.

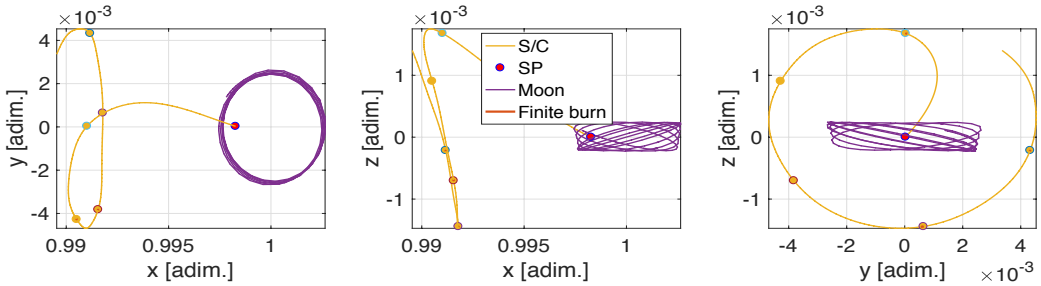

(b) Family σ.

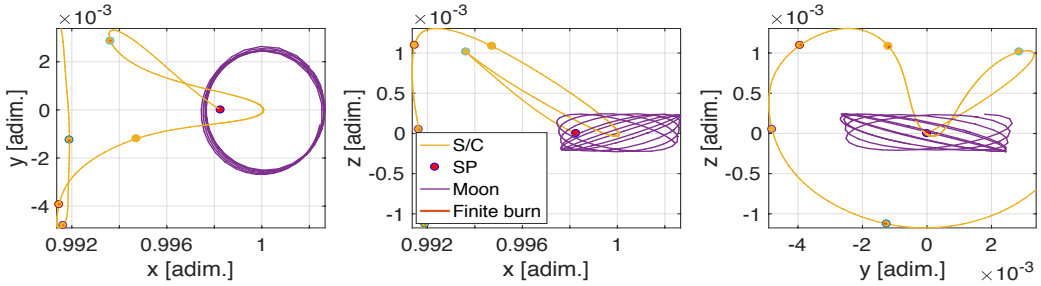

(c) Family EGA (Earth gravity assist).

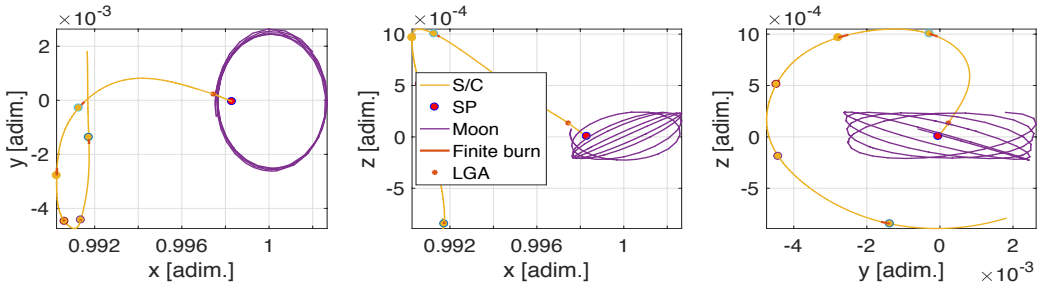

(d) Family σ with lunar encounter.

Figure 6: Solutions departing from L_1 LPO (batch 1/2).

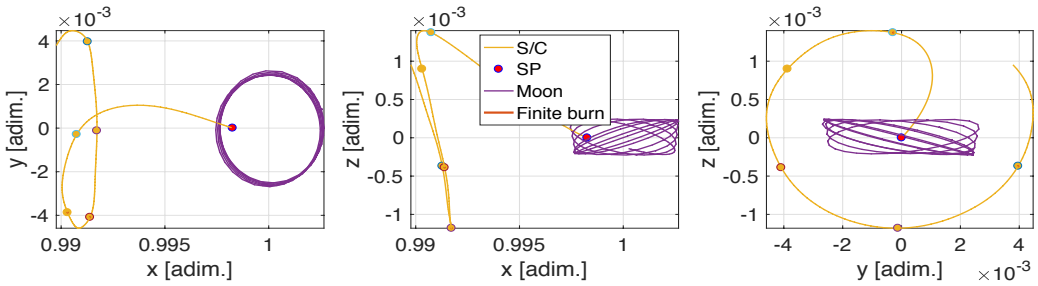

(a) Minimum Δv.

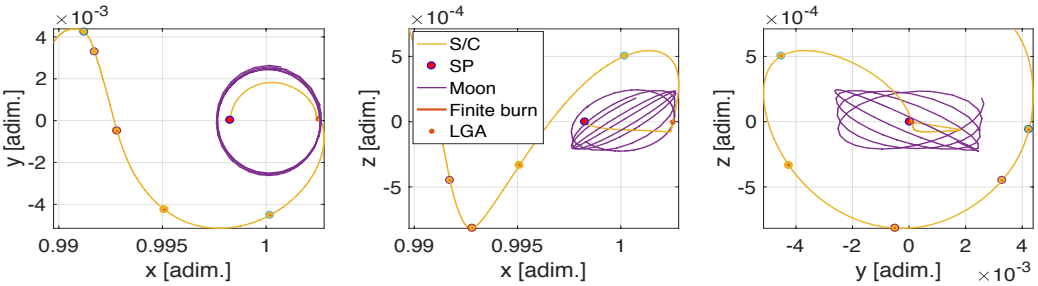

(b) Low-altitude lunar encounter.

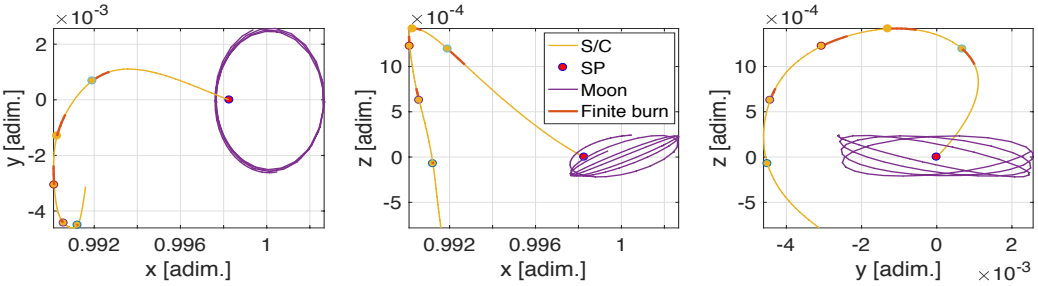

(c) Minimum ToF.

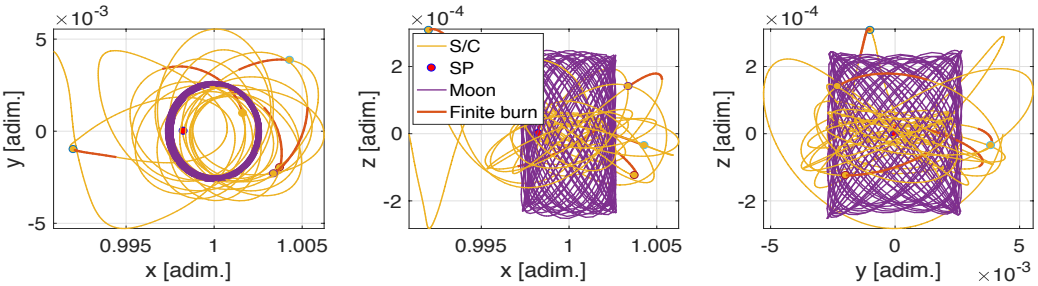

(d) Maximum ToF.

Figure 7: Solutions departing from L_1 LPO (batch 2/2).

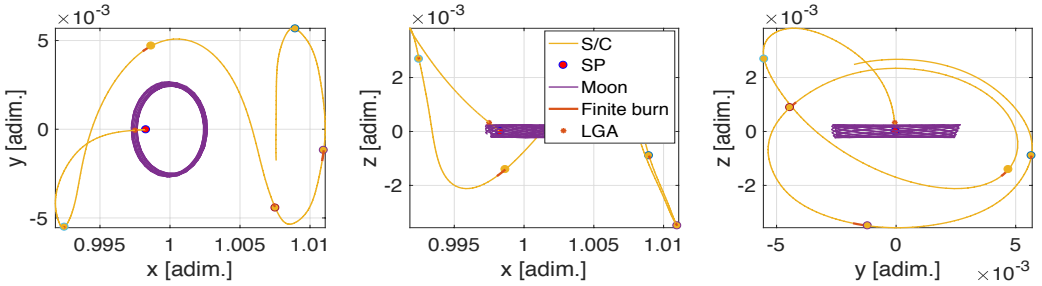

(a) Family Ω.

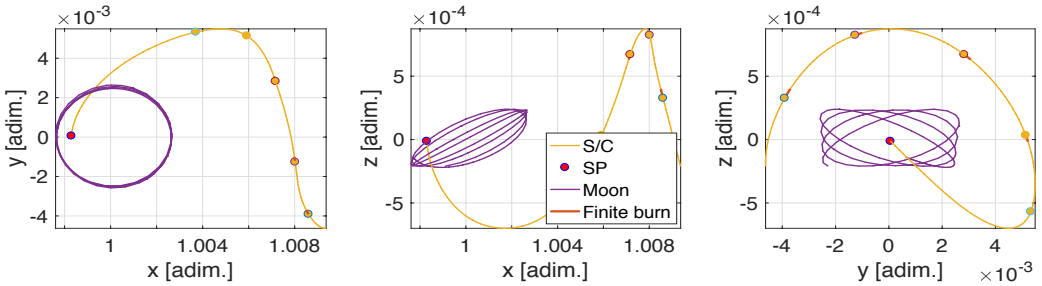

(b) Family σ.

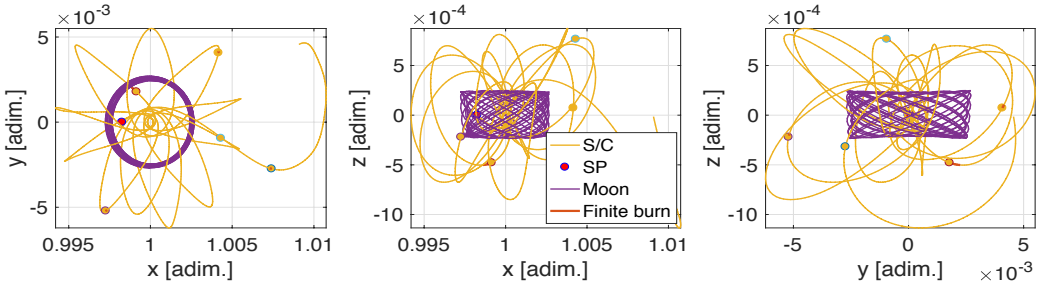

(c) Family EGA.

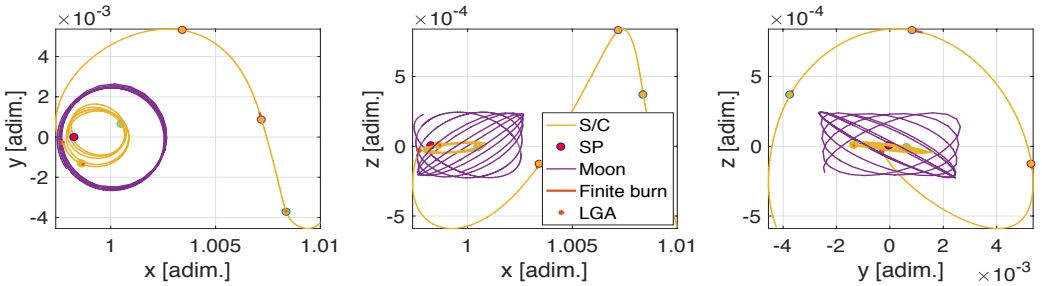

(d) Family σ with lunar encounter.

Figure 8: Solutions departing from L_2 LPO (batch 1/2).

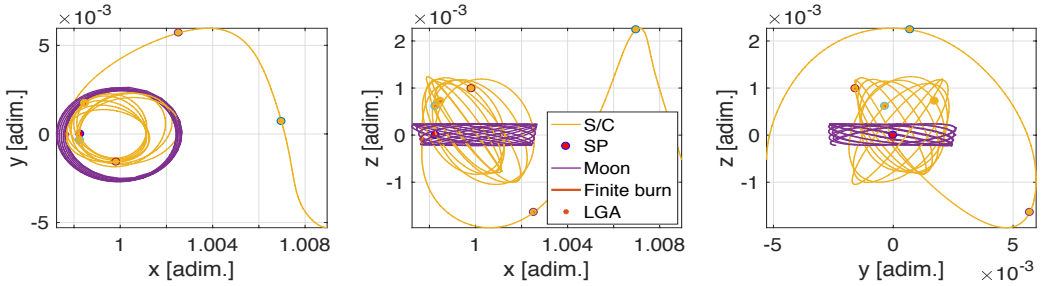

(a) Minimum Δv.

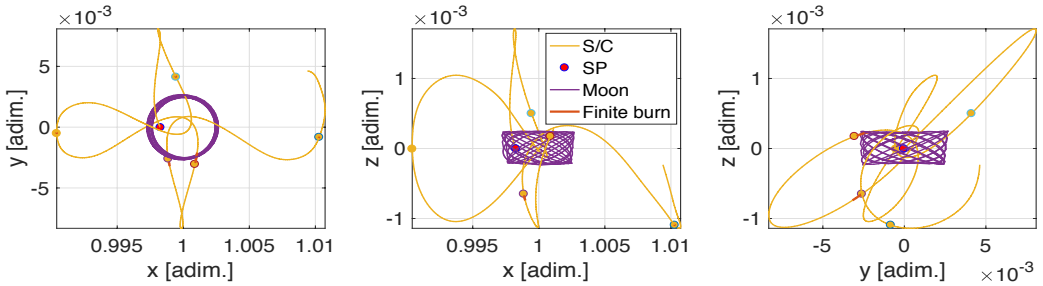

(b) Propeller.

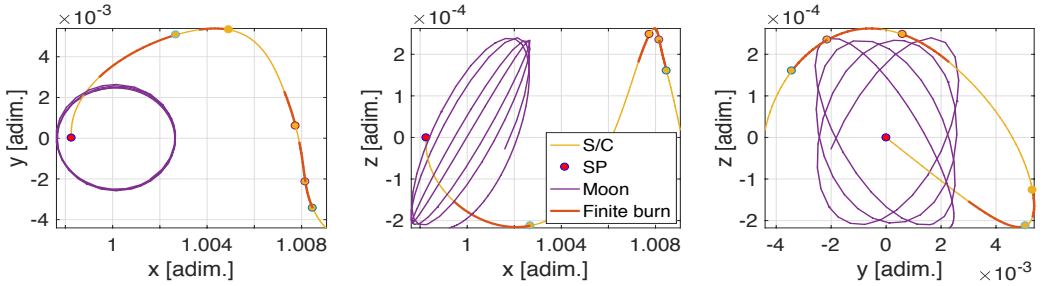

(c) Minimum ToF.

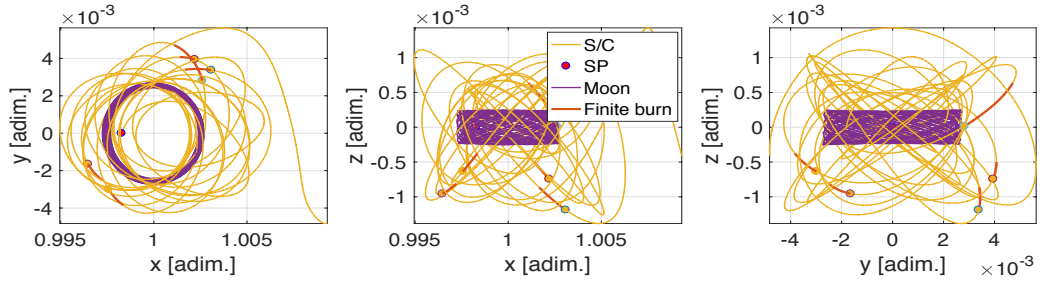

(d) Maximum ToF.

Figure 9: Solutions departing from L_2 LPO (batch 2/2).

3. Close lunar gravity assists (LGA) may benefit the overall fitness of the solution, either in terms of time of flight or fuel consumption, but it is not required for optimality.

4. As expected for ultra-low control authority spacecraft, the time spent thrusting is a significant amount of the total ToF. The vast majority of SP transfers displays slow-varying control azimuth and elevation during engine firing. This is beneficial for attitude pointing during the maneuver continued execution.

5. The sheer number of FBM transfers to the SP provides sufficient diversity in the solution and control space to allow for a robust feasibility analysis and to draw reliable statistic conclusions.

4.2. LISA Pathfinder mission extension to the Sun–Earth saddle point

The mission extension of LISA Pathfinder is considered as case study. As a technology demonstrator for the gravitational wave observatory mission Laser Interferometer Space Antenna (LISA), LPF is also equipped with a gravity gradiometer consisting of two freely falling test masses, separated by a baseline of just under 40 cm, whose position is measured through laser interferometry with picometer resolution. Simulations have shown that this technology, with the level of accuracies reached, is an ideal apparatus to collect data at the SP, for a possible confirmation of the MOND/TeVeS theory (Trenkel and Kemble, 2009; Trenkel et al., 2012; Trenkel and Wealthy, 2014).

LISA Pathfinder was flying about Sun–Earth L_1 into a Lissajous orbit and had a residual control capability after nominal and extended missions. This residual capability can be estimated into a Δv budget of $\sim$ 1 m/s. The residual, potential action cannot be modeled as producing instantaneous velocity changes, as the maximum thrust level of the cold-gas thrusters is in the order of 100 μN each, and thus applying velocity changes may require maneuvering for several days. LPF is then an ultra low thrust spacecraft that flies into a highly unstable environment. Table 5 provides the set-up parameters to simulate LPF mission extension[5].

The available estimation for the end-of-operation state (position, velocity) is taken as initial condition, and the cold gas propulsion available on the

[5] Δv budget at beginning of life (BoL) for LPF was 3.8 m/s (Table 6.2 of LPF CReMA (Landgraf et al., 2014)); the one reported in Table 5 is assumed.

LPF Science Module is considered as primary propulsion. Several mission extension options are designed and validated, and their implementation is discussed. The real ephemeris of LPF, representing its accurate position and velocity, has been provided by ESA as a CCSDS OEM file (Consultative Committee for Space Data Systems Orbit Ephemeris Message file). The OEM file has been converted into a SPICE[6] kernel for use in the current work. The ephemeris data for LPF ranges from 2016 September 18 16:49:36.497 Barycentric Dynamical Time (TDB) to 2018 March 13 06:14:47.510 TDB. LPF trajectory is plotted in Figure 10 in the Sun–Earth rotating frame. The LPF orbit roughly retraces a $A_z = 400,000$ km amplitude halo.

4.2.1. LISA Pathfinder transfer design

The trajectory of LPF mission extension to the saddle point is designed with the following methodology.

1. An exploration of the solution space is performed starting from the real

Table 5: Dimensioned parameters for the LISA Pathfinder S/C at EoL.

m_0 [kg]	$T_{\max}$ [mN]	I_{sp} [s]	$\Delta v_{\max}$ [m/s]
500	1	60	1

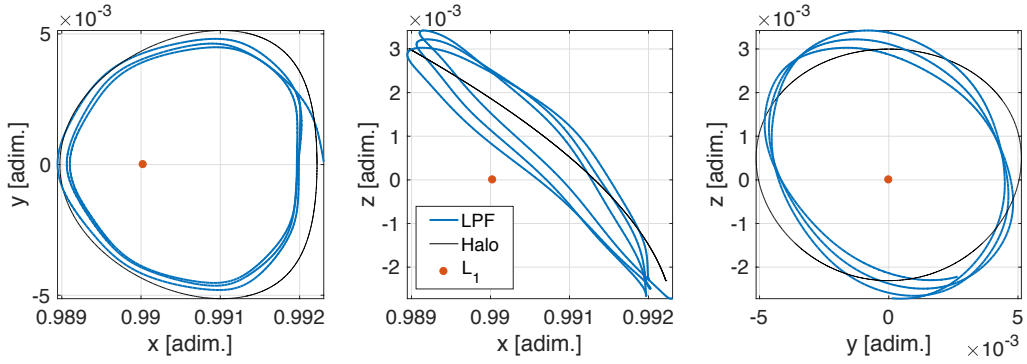

Figure 10: LISA Pathfinder trajectory.

[6]SPICE is NASA's Observation Geometry and Information System for Space Science Missions (Acton Jr, 1996; Acton Jr et al., 2018). `https://naif.jpl.nasa.gov/naif`; last downloaded on February 7, 2018.

LPF ephemeris (for more details on the exploration see Topputo et al. (2018b)). The sole initial epoch, t_0, is sufficient to fully characterize the initial conditions for the exploration, and a fine search is applied to the variable t_0. The grid search bounds are set to $t_0 \in$ [30 March 2017 00:00:00.0 , 28 June 2017 00:00:00.0] TDB. A 90-day search grid is deemed to well represent the LPF-to-SP dynamics. Moreover, these dates are compatible with a real implementation of the ultra-low transfer as mission extension for LPF.

2. Solutions, output of the exploration campaign, are used as initial guesses for a precise (meters threshold) targeting of the real SP with a multiple burn multiple shooting technique (Topputo et al., 2018c; Dei Tos and Topputo, 2019). Five impulsive maneuvers are used to drive LPF to fly through the saddle point.

3. Impulsive maneuvers, giving rise to optimal LPF-to-SP transfers, are spread into finite burn arcs after application of Algorithm 1.

In Table 6, some important parameters of the LPF-to-SP transfers are summarized. Our design follows a three-step approach: Exploration, Optimization, Finite-burn conversion. In particular, 123 ballistic SP fly-throughs have been found approaching a $10,000$ km sphere around the SP (exploration), of which 93 have been optimized for fine SP targeting with impulsive maneuvers (optimization). Among the latter, 73 solutions have been refined in the RPRnBP with propelled arcs (finite-burn conversion). Attitude rates

Table 6: Trajectory design summary for the LPF mission extension case.

Phase	Metrics	LPF
Exploration	#	123
Optimization	#	93
	Total Δv [m/s]	6.88 ± 4.79
	Deterministic SP miss distance [mm]	0.7 ± 1.3
Finite burn	#	73
	Propellant consumed Δm [kg]	5.00 ± 2.13

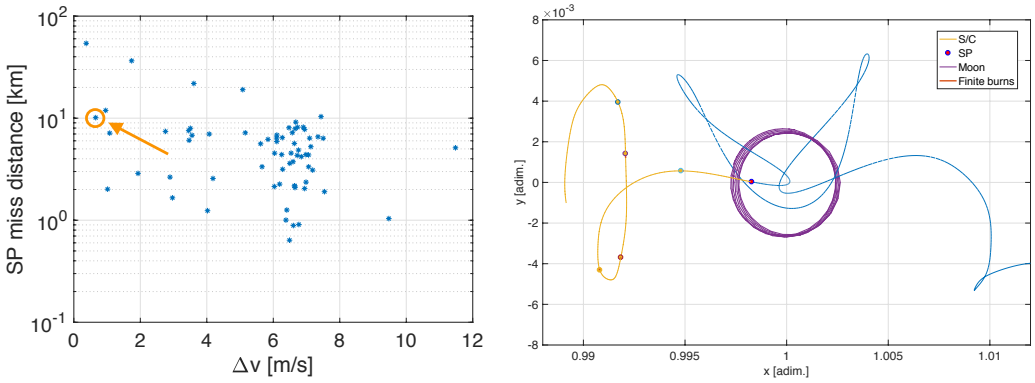

(a) Solution space.

(b) Departure: 2017/6/21 10:54:42.408 TDB. Arrival: 2018/1/15 10:32:24.516 TDB.

Figure 11: LISA Pathfinder transfers to the SP.

in the order of few degrees per day are necessary for the finite-burn maneuvers, compatibly with the performances of the LPF attitude subsystem. The totality of solutions that have been found from the LPF initial trajectory belong to family δ (see Section 4.1). This predominance of δ-type transfers is due to the relatively high amplitude Lissajous orbit LPF was flying along. Figure 11a displays the whole set of preliminary solutions. The solution corresponding to $\Delta v = 0.657$ m/s and ToF = 208 days is plotted in Figure 11b as a feasible deterministic example. The navigation assessment is also shown later for this solution. The solid line on the left part of the plot is the direct SP transfer, whereas the darker solid line is the orbit behavior after the SP fly-through. This trajectory is self-disposing, that is, after two close Earth encounters LPF would permanently leave the Earth–Moon system and not return in the mid-term.

4.2.2. LISA Pathfinder flyability analysis

Simulations for the navigation assessment are performed using correlated process noises (see Section 3.2.3) and range and range-rate measurements from Cebreros ground station, using the error values reported in Table 2, a large, initial uncertainty of 100 km in each component of position, 1 m/s in each component of velocity, and 0.1 kg in mass; a mapping time of 0.25 days; and a maximum visibility windows frequency of once per week.

The navigation assessment described in Section 3 is applied to the 73 LPF-to-SP transfers found. Results for the LISA Pathfinder transfer shown

in Figure 11b are displayed in Figures 12–18. More in detail, Figure 12 shows the declination during the entire transfer. This angle becomes relevant when close to zero, where it can severely deteriorate the determination of the spacecraft angular position based on Doppler data.

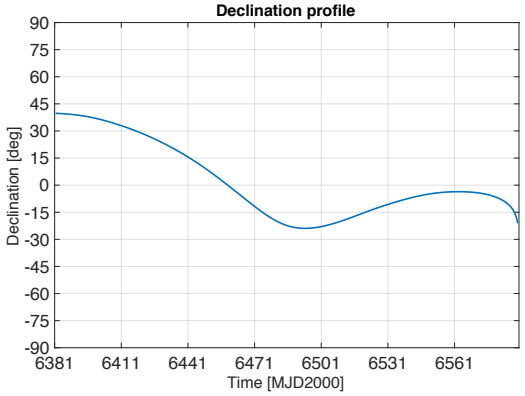

Figure 12: Declination angle profile.

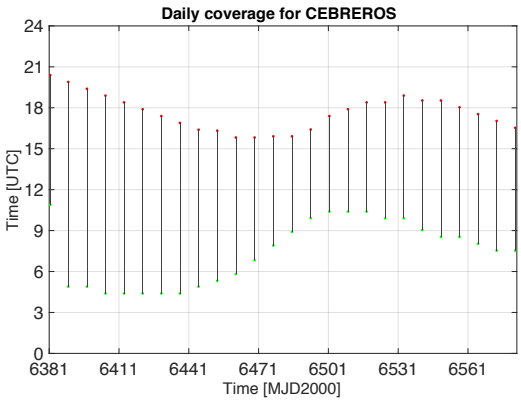

Figure 13: Daily coverage from Cebreros.

As shown in Figure 13, long visibility windows ($t_c \geq 12$ hours) are available at the beginning of the transfer, whereas a progressive reduction of their duration is found towards the end, i. e., close to the SP, due to the passage across the equator, which affects LPF elevation with respect to Cebreros. Within these coverage windows, simulated range and range-rate measurements are generated as shown in Figures 14a–14b, respectively.

Figures 15a–15b illustrate the results of the covariance analysis and, in particular, the achievable knowledge accuracy of the spacecraft state along

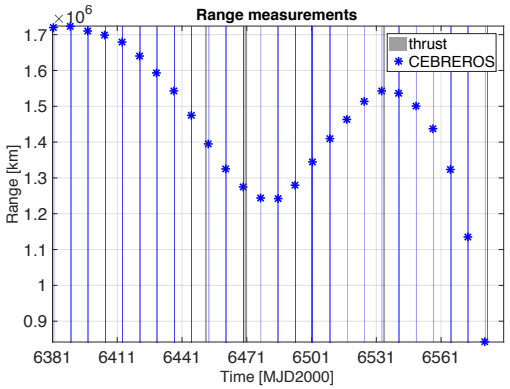

(a) Range measurements.

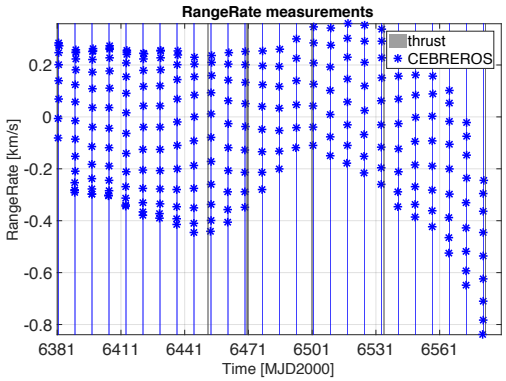

(b) Doppler measurements.

Figure 14: Radiometric measurements within coverage windows.

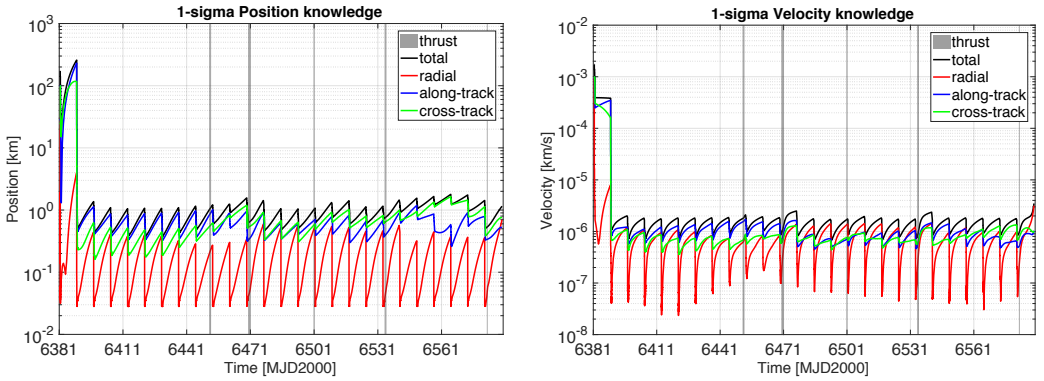

(a) Achievable position knowledge. (b) Achievable velocity knowledge.

Figure 15: LISA Pathfinder state knowledge.

Table 7: 1σ position and velocity knowledge values at SP passage.

Component	Position [km]	Velocity [km/s]
Radial	6.962e-01	3.168e-06
Along-track	5.261e-01	1.028e-06
Cross-track	7.554e-01	1.027e-06

the transfer. As shown, after an initial improvement in the level of accuracy, a limit is generally reached due to the effects of process and measurement noises. The values of 1σ position and velocity knowledge at the SP passage (i. e., at the end of the transfer), are reported for each component in Table 7. Note that the 1σ values in Table 7 strongly depend on the measurement interval. We expect that tuning the measurement interval may lead to an improvement in the radial position and radial velocity knowledge at saddle point passage. Note that from Figure 15b and Table 7, the achieved radial velocity is slightly lower than the Doppler noise of 0.03 mm/s. This occurs because the Doppler noise is factored in the SRIF as a Gaussian process with zero mean, not as a constant noise with random direction.

The results of Monte Carlo analyses, using 100 samples and based on the guidance assumptions described in Section 3.2.5, are reported in Figures 16a–16b. A mean Δv of 2.538 m/s is found, with a standard deviation of 1.114 m/s. However, as shown in Figure 16b and summarized in Table 8, an higher value is required, i. e., 4.533 m/s, for a 95% confidence level. Thus, the size of

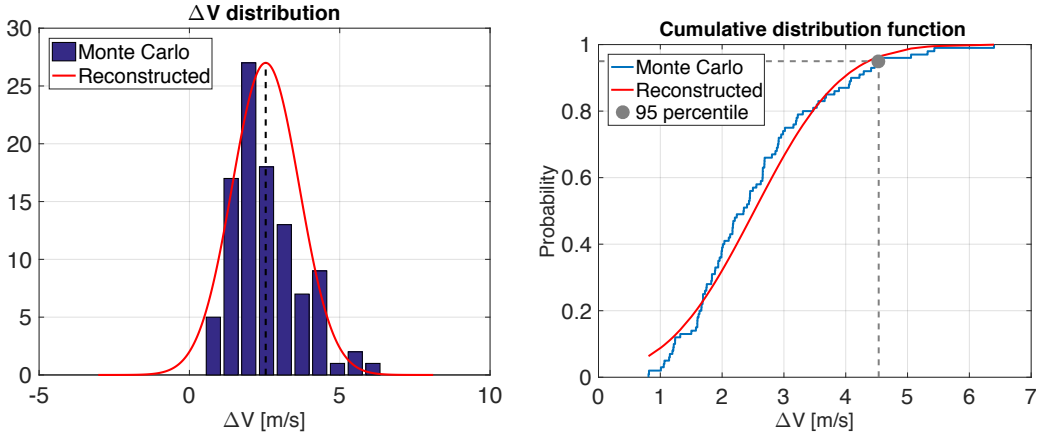

(a) Probablity density fuction. (b) Cumulative distribution function.

Figure 16: Navigation Δv distribution.

Table 8: Statistical Δv required for navigation.

Δv_{nav}	Mean	Standard deviation	95 percentile
Value [m/s]	2.538	1.114	4.533

Δv needed to navigate the nominal trajectory may be very large, if compared with the nominal Δv, even an order of magnitude larger as in this case.

As already mentioned in Section 3.2.5, resulting TCM have to be applied using the LPF cold gas propulsion system. Figure 17 reports the time needed to apply the required Δv changes, computed a posteriori by using the actual values of mass, thrust, and specific impulse. Note in particular how, the time needed for the first correction maneuver overcomes the $t_{\max}$, in case of TCM frequency equal to once per week. On the contrary, changing the frequency, e. g., one maneuver every two weeks, leads to a general increment in the size of correction maneuvers, due to the larger dispersions reached during the propagation. However, it also ensures a larger time for the application of TCM before the next OD. In this case all the maneuvers are below the maximum threshold and could therefore be implemented in a real scenario.

4.2.3. Critical analysis

The initial uncertainties in position and velocities considered in the feasibility analysis (Section 4.2.2) are 100 km and 1 m/s, respectively. These

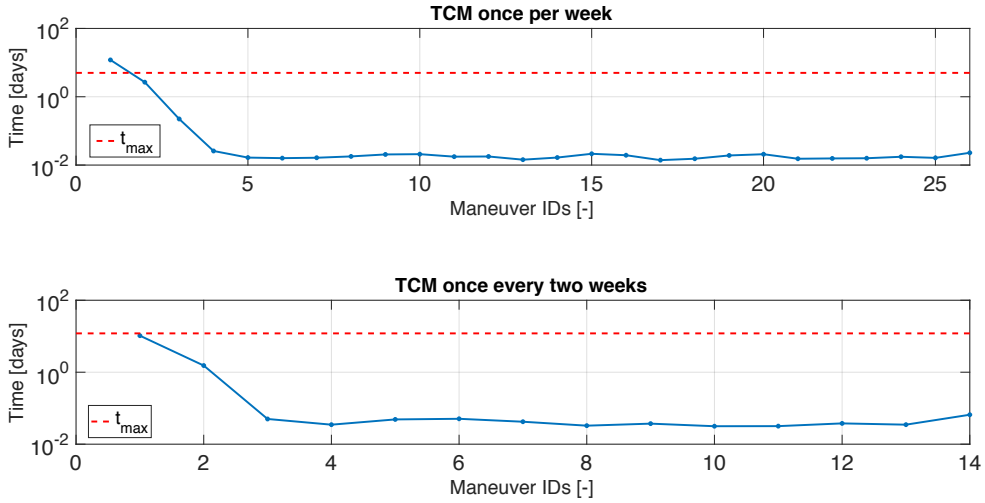

Figure 17: Time required for the implementation of correction maneuvers.

values are more typical of post-launch conditions, and hardly apply to a spacecraft that is flying on a regular basis in the near-Earth environment. The relatively high statistical cost to navigate the nominal transfer reported in Table 8 is mostly due to this assumption, because the initial uncertainty determines how far the generated Monte Carlo samples are with respect to the nominal transfer trajectory, which in turn affects the size of the TCM. A parametric analysis was performed by varying the size of this initial uncertainty. Seven cases, ranging from A to G, were considered, with the initial uncertainty in position and velocity given in Table 9. Figure 18 reports the results obtained for different cases. As expected, a smaller initial dispersion leads to smaller correction maneuvers and vice-versa. This means that starting the transfer with a good level of position and velocity knowledge may drastically reduce the value of Δv required to navigate the nominal trajectory and eventually affect the feasibility of transfer solutions.

For LPF at EoL condition, it is sound to consider a circumstance in which the initial position and velocity uncertainties are between case E and F: 5-10 km and 0.05-0.1 m/s, respectively. The 95-percentile navigation cost associated to case E and F is 0.48 m/s and 0.30 m/s, respectively. When summed to the deterministic cost for the transfer shown throughout Section 4.2.2 (0.657 m/s, see Figure 11), it yields a total cost of 0.957–1.137 m/s. Although at the limit of the budget, this cost is compatible with the estimated residual budget in Table 5, which indicates evidence for the feasibility of the

LISA Pathfinder transfer to the Sun–Earth saddle point. Having disposed LPF on July 18 2017, therefore not opting for the opportunistic mission extension described in this paper, may have represented a missed opportunity.

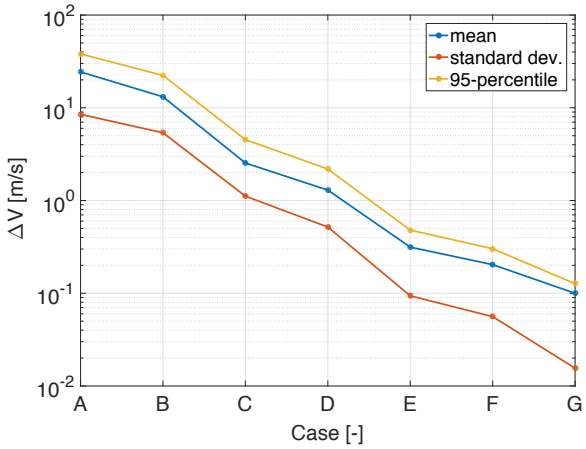

Figure 18: Navigation cost for several case with different initial dispersion.

Table 9: Cases on initial dispersion.

Case	σ_r [km]	σ_v [m/s]
A	10000	10
B	500	5
C	100	1
D	50	0.5
E	10	0.1
F	5	0.05
G	1	0.01

5. Conclusions

A method to convert impulsive maneuvers into finite burn arcs is presented. The method is applied to the case of LISA Pathfinder transfer to the Sun–Earth gravitational saddle point with very promising results, both in terms of convergence and in terms of optimality of the solutions. Many transfers are found from the Sun–Earth libration point region, which feature reasonable time of flight and very low Δv consumption, from few centimeters per second to 10 m/s, compatibly with the limited control authority of the spacecraft.

Navigation analysis results have shown that some limitations do exist, due to the level of Δv required to keep the spacecraft on the nominal path. In particular, it is found that the sizes of correction maneuvers are highly influenced by the frequency chosen for the guidance process as well as by the initial dispersion of the spacecraft state. Therefore, LPF could haven been moved to the SP only if the initial dispersion was reduced to a value smaller than 10 km on each position component and smaller than 0.1 m/s on each velocity component. These values are compatible with ESA current deep-

space tracking capabilities. With these conditions, a guidance frequency of one control maneuver per week would have been sufficient. For larger initial dispersion values, the size of correction maneuvers rapidly increases, with a consequent need to reduce the guidance frequency to once every two weeks or even lower values, to ensure their proper implementation with the on-board thrusters. Nonetheless, in these cases the transfer feasibility could still be jeopardized, due to high level of Δv required.

This work shows evidence of feasibility to fly and navigate LISA Pathfinder towards the Sun–Earth saddle point, exploiting the chaotic dynamics of a high-fidelity dynamical model. Nevertheless, LPF was disposed on July 2017, and the result of the present work were not used.

Acknowledgments

The work described in this paper has been conducted under ESA Contract No. 4000118201/16/F/MOS. The authors would like to acknowledge Masaki Nakamiya, Gonçalo Aguiar, Erind Veruari, and Srikara Cherukuri for their valuable contribution.

References

Acton Jr, C., 1996. Ancillary data services of NASA's navigation and ancillary information facility. Planetary and Space Science 44, 65–70. doi:10.1016/0032-0633(95)00107-7.

Acton Jr, C., Bachman, N., Semenov, B., Wright, E., 2018. A look towards the future in the handling of space science mission geometry. Planetary and Space Science 150, 9–12. doi:10.1016/j.pss.2017.02.013.

Bekenstein, J.D., 2004. Relativistic gravitation theory for the modified Newtonian dynamics paradigm. Physical Review D 70, 083509.1–28. doi:10.1103/PhysRevD.70.083509.

Bekenstein, J.D., Magueijo, J., 2006. Modified Newtonian dynamics habitats within the solar system. Physical Review D 73, 103513.1–14. doi:10.1103/PhysRevD.73.103513.

Belbruno, E., Miller, J.K., 1993. Sun-perturbed Earth-to-Moon transfers with ballistic capture. Journal of Guidance, Control, and Dynamics 16, 770–775. doi:10.2514/3.21079.

Bowell, E., Virtanen, J., Muinonen, K., Boattini, A., 2002. Asteroid orbit computation, in: Bottke, W.F.J., Cellino, A., Paolicchi, P., Binzel, R.P. (Eds.), Asteroids III. University of Arizona Press, pp. 27–43.

Bryson, A.E., 1975. Applied optimal control: optimization, estimation and control. CRC Press.

Cox, A., Howell, K.C., 2016. Transfers to a Sun–Earth saddle point: An extended mission design option for LISA Pathfinder, in: Advances in the Astronautical Sciences, pp. 653–668.

Crassidis, J.L., Markley, F.L., 2003. Unscented filtering for spacecraft attitude estimation. Journal of Guidance, Control, and Dynamics 26, 536–542. doi:10.2514/2.5102.

Dei Tos, D.A., 2018. Trajectory optimization of limited control authority spacecraft in high-fidelity models. Ph.D. thesis. Politecnico di Milano, Milano, Italy. URL: https://www.politesi.polimi.it/handle/10589/137086, doi:10.13140/RG.2.2.15099.00804.

Dei Tos, D.A., Topputo, F., 2017. Trajectory refinement of three-body orbits in the real solar system model. Advances in Space Research 59, 2117–2132. doi:10.1016/j.asr.2017.01.039.

Dei Tos, D.A., Topputo, F., 2019. High-fidelity trajectory optimization with application to saddle-point transfers. Journal of Guidance, Control, and Dynamics, accessed February 19, 2019 doi:10.2514/1.G003838.

Fabacher, E., Kemble, S., Trenkel, C., Dunbar, N., 2013. Multiple Sun–Earth saddle point flybys for LISA Pathfinder. Advances in Space Research 52, 105–116. doi:10.1016/j.asr.2013.02.005.

Farquhar, R.W., Dunham, D.W., Guo, Y.P., McAdams, J.V., 2004. Utilization of libration points for human exploration in the Sun–Earth–Moon system and beyond. Acta Astronautica 55, 687 – 700. doi:10.1016/j.actaastro.2004.05.021.

Farquhar, R.W., Muhonen, D.P., Newman, C.R., Heubergerg, H.S., 1980. Trajectories and Orbital Maneuvers for the First Libration-Point Satellite. Journal of guidance, control, and dynamics 3, 549–554. doi:10.2514/3.56034.

Galianni, P., Feix, M., Zhao, H.S., Horne, K., 2012. Testing quasilinear modified Newtonian dynamics in the solar system. Phys. Rev. D 86, 044002. doi:10.1103/PhysRevD.86.044002.

Givens, W., 1958. Computation of plain unitary rotations transforming a general matrix to triangular form. Journal of the Society for Industrial and Applied Mathematics 6, 26–50. doi:10.1137/0106004.

Gómez, G., Masdemont, J., Mondelo, J., 2002. Solar system models with a selected set of frequencies. Astronomy and Astrophysics 390, 733–750. doi:10.1051/0004-6361:20020625.

Guo, Y.N., Hawkins, M., Wie, B., 2013. Applications of Generalized Zero-Effort-Miss/Zero-Effort-Velocity Feedback Guidance Algorithm. Journal of Guidance, Control, and Dynamics 36, 810–820. doi:10.2514/1.58099.

Hees, A., Famaey, B., Angus, G.W., Gentile, G., 2016. Combined solar system and rotation curve constraints on MOND. Monthly Notices of the Royal Astronomical Society 455, 449–461. doi:10.1093/mnras/stv2330.

Landgraf, M., Renk, F., de Vogeleer, B., Boutonnet, A., 2014. LISA Pathfinder Consolidated Report on Mission Analysis. European Space Agency (ESA), CReMA, S2-ESC-RP-5001. ESA.

Milgrom, M., 1983. A modification of the Newtonian dynamics as a possible alternative to the hidden mass hypothesis. Astrophysical Journal 270, 365–370. doi:10.1086/161130.

Milgrom, M., 2008. The MOND paradigm. arXiv preprint astro-ph/0801.3133 .

Mingotti, G., Topputo, F., 2011. Ways to the Moon: A survey, in: Advances in the Astronautical Sciences, pp. 2531–2547.

Modenini, D., Zannoni, M., Tortora, P., 2017. Retrodictor-corrector filter. Journal of Guidance, Control, and Dynamics 40, 2330–2334. doi:10.2514/1.G002969.

Montenbruck, O., Gill, E., 2000. Satellite orbits: models, methods and applications. Springer Science & Business Media.

Ocampo, C., Munoz, J.P., 2010. Variational equations for a generalized spacecraft trajectory model. Journal of guidance, control, and dynamics 33, 1615–1622. doi:10.2514/1.46953.

Park, R.S., Scheeres, D.J., 2006. Nonlinear mapping of gaussian statistics: Theory and applications to spacecraft trajectory design. Journal of Guidance, Control, and Dynamics 29, 1367–1375. doi:10.2514/1.20177.

Sanders, R.H., 2007. Modified gravity without dark matter, in: Papantonopoulos, L. (Ed.), The Invisible Universe: Dark Matter and Dark Energy. Lecture Notes in Physics, vol. 720, Springer, Berlin, Heidelberg, pp. 375–402. doi:10.1007/978-3-540-71013-4_13.

Sanders, R.H., McGaugh, S.S., 2002. Modified Newtonian dynamics as an alternative to dark matter. Annual Review of Astronomy and Astrophysics 40, 263–317. doi:10.1146/annurev.astro.40.060401.093923.

Senent, J., Ocampo, C., Capella, A., 2005. Low-thrust variable-specific-impulse transfers and guidance to unstable periodic orbits. Journal of Guidance, Control, and Dynamics 28, 280–290. doi:10.2514/1.6398.

Tapley, B.D., Schutz, B.E., Born, G.H., 2004. Statistical orbit determination. Academic Press.

Topputo, F., Belbruno, E., 2015. Earth–Mars transfers with ballistic capture. Celestial Mechanics and Dynamical Astronomy 121, 329–346. doi:10.1007/s10569-015-9605-8.

Topputo, F., Dei Tos, D.A., Mani, K.V., Ceccherini, S., Giordano, C., Franzese, V., Wang, Y., 2018a. Trajectory design in high-fidelity models, in: 7th International Conference on Astrodynamics Tools and Techniques (ICATT), pp. 1–9.

Topputo, F., Dei Tos, D.A., Rasotto, M., Nakamiya, M., 2018b. The Sun–Earth saddle point: characterization and opportunities to test general relativity. Celestial Mechanics and Dynamical Astronomy 130, 33. doi:10.1007/s10569-018-9824-x.

Topputo, F., Dei Tos., D.A., Rasotto, M., Renk, F., 2018c. Design and feasibility assessment of ultra low thrust trajectories to the Sun-Earth saddle

point, in: 2018 Space Flight Mechanics Meeting, AIAA SciTech Forum, (AIAA 2018-1691). doi:10.2514/6.2018-1691.

Topputo, F., Zhang, C., 2014. Survey of direct transcription for low-thrust space trajectory optimization with applications. Abstract and Applied Analysis 2014. doi:10.1155/2014/851720.

Trenkel, C., Kemble, S., 2009. Gravitational science with LISA Pathfinder. Journal of Physics: Conference Series 154, 012002. doi:10.1088/1742-6596/154/1/012002.

Trenkel, C., Kemble, S., Bevis, N., Magueijo, J., 2012. Testing modified Newtonian dynamics with LISA Pathfinder. Advances in Space Research 50, 1570–1580. doi:10.1016/j.asr.2012.07.024.

Trenkel, C., Wealthy, D., 2014. Effect of LISA Pathfinder spacecraft self-gravity on anomalous gravitational signals near the Sun–Earth saddle point predicted by quasilinear MOND. Physical Review D 90, 084037.1–22. doi:10.1103/PhysRevD.90.084037.

Yarnoz, D.G., Jehn, R., Croon, M., 2006. Interplanetary navigation along the low-thrust trajectory of BepiColombo. Acta Astronautica 59, 284–293. doi:10.1016/j.actaastro.2006.02.028.